

Overview of quantitative susceptibility mapping

Andreas Deistung^{a*}, Ferdinand Schweser^{b,c} and Jürgen R. Reichenbach^{a,d*}

Magnetic susceptibility describes the magnetizability of a material to an applied magnetic field and represents an important parameter in the field of MRI. With the recently introduced method of quantitative susceptibility mapping (QSM) and its conceptual extension to susceptibility tensor imaging (STI), the non-invasive assessment of this important physical quantity has become possible with MRI. Both methods solve the ill-posed inverse problem to determine the magnetic susceptibility from local magnetic fields. Whilst QSM allows the extraction of the spatial distribution of the bulk magnetic susceptibility from a single measurement, STI enables the quantification of magnetic susceptibility anisotropy, but requires multiple measurements with different orientations of the object relative to the main static magnetic field. In this review, we briefly recapitulate the fundamental theoretical foundation of QSM and STI, as well as computational strategies for the characterization of magnetic susceptibility with MRI phase data. In the second part, we provide an overview of current methodological and clinical applications of QSM with a focus on brain imaging. Copyright © 2016 John Wiley & Sons, Ltd.

Keywords: magnetic susceptibility; quantitative susceptibility mapping; susceptibility tensor imaging; functional MRI; multiple sclerosis

INTRODUCTION

Quantitative susceptibility mapping (QSM) together with its more recent extension to susceptibility tensor imaging (STI) are both relatively new MRI techniques that aim to extract the spatial susceptibility distribution of objects or tissues from the measured MRI phase or local field data by solving a known inverse problem. Since the earliest days of MRI, the quantification of magnetic susceptibility was considered to be an important goal, as it was anticipated that magnetic susceptibility, similar to T_1 and T_2 relaxation constants, could be useful to characterize diseased tissue. Already in 1984, ways to measure and interpret the effect of tissue susceptibility variations from MRI data had been investigated in normal human subjects and

patients (1), and were quickly extended and refined in the following years (2–8).

In rather general terms, magnetic susceptibility is the physical quantity that describes the change in magnetization of a material in response to an applied magnetic field. Being an important source of MR image artifacts, the property has long been considered as a nuisance rather than a benefit because even small magnetic susceptibility variations of only a few parts per million (ppm), such as the susceptibility difference between air and brain tissue, lead to long-ranging field distortions that can cause MRI signal voids and/or geometrical image distortions (9,10). Indeed, materials with large susceptibilities (on the order of one or larger), i.e. materials that respond very strongly to an applied magnetic field, must be excluded strictly from the MRI

* Correspondence to: A. Deistung and J. R. Reichenbach, Medical Physics Group, Institute of Diagnostic and Interventional Radiology, Jena University Hospital – Friedrich Schiller University Jena, Philosophenweg 3, 07743 Jena, Germany.
E-mail: andreas.deistung@med.uni-jena.de; juergen.reichenbach@med.uni-jena.de

a A. Deistung, J. R. Reichenbach
Medical Physics Group, Institute of Diagnostic and Interventional Radiology, Jena University Hospital – Friedrich Schiller University Jena, Jena, Germany

b F. Schweser
Buffalo Neuroimaging Analysis Center, Department of Neurology, Jacobs School of Medicine and Biomedical Sciences, The State University of New York at Buffalo, NY, USA

c F. Schweser
MRI Clinical and Translational Research Center, Jacobs School of Medicine and Biomedical Sciences, The State University of New York at Buffalo, NY, USA

d J. R. Reichenbach
Michael Stifel Center for Data-driven and Simulation Science Jena, Friedrich Schiller University Jena, Jena, Germany

Abbreviations used: AD, Alzheimer's disease; bSSFP, balanced steady-state free precession; CAIPI, controlled aliasing in parallel imaging; CG, conjugate gradient; CMRO₂, cerebral metabolic oxygenation rate; CNR, contrast-to-noise ratio; COSMOS, calculation of susceptibility through multiple orientation sampling; CSF, cerebrospinal fluid; CT, computed tomography; DBS, deep brain stimulation; DTI, diffusion tensor imaging; EPI, echo planar imaging; FIRST, FMRIB's integrated registration and segmentation tool; FLAIR, fluid-attenuated inversion recovery; fMRI, functional MRI; FOV, field of view; fQSM, functional quantitative susceptibility mapping; FRDA, Friedreich's ataxia; GLTA, generalized Lorentzian tensor approach; GM, gray matter; GRE, gradient echo; HEIDI, homogeneity-enabled incremental dipole inversion; LSQR, least-squares QR decomposition; MEDI, morphological-enabled dipole inversion; MS, multiple sclerosis; PD, Parkinson's disease; PDF, projection onto dipole fields; PET, positron emission tomography; PIXE, proton-induced X-ray emission; ppb, parts per billion; ppm, parts per million; QSM, quantitative susceptibility mapping; R_2 , effective transverse relaxation rate; SCA, spinocerebellar ataxia; SD, steepest descent; SHARP, sophisticated harmonic artifact reduction for phase data; SN, substantia nigra; SNR, signal-to-noise ratio; SQUID, superconducting quantum interference device; STI, susceptibility tensor imaging; SWI, susceptibility-weighted imaging; TBI, traumatic brain injury; TKD, thresholded k-space division; VOI, volume of interest; WASSR, water saturation shift referencing; WM, white matter.

magnet room as they present a risk of injury or even death to patients because of the associated magnetic forces and torques exerted, e.g. on implants and external devices (11,12). However, the small magnetic susceptibilities of tissues, typically only $\pm 20\%$ of the susceptibility of water ($\chi_{\text{H}_2\text{O}} = -9.05 \times 10^{-6}$ in SI units) (12), cause only very subtle field distortions, which offer unique possibilities for the creation of image contrast. This has, for instance, been performed with susceptibility-weighted imaging (SWI), an MRI method that specifically multiplies magnitude and phase information obtained from a T_2^* -weighted gradient echo (GRE) sequence (13). The enhancement of susceptibility contrast in this way enables the unique delineation of the human cerebral venous vessel network with high spatial resolution *in vivo* because of the tiny susceptibility difference between venous blood and brain tissue (13,14). Other examples include functional MRI (fMRI), where the difference in hemoglobin's magnetic susceptibility between the oxygenated and deoxygenated state contributes to the induced signal changes (15). In addition, the characterization and quantification of magnetic susceptibility by means of MRI data have helped to distinguish between the presence of calcium and blood deposits in brain tissue (16–18), as well as the assessment of iron content in brain structures (19–22) and the visualization of abnormal venous vessels (23).

The advent of ultra-high-field MRI and its accompanying increased sensitivity against magnetic susceptibility differences not only resulted in superb anatomical contrast on T_2^* -weighted magnitude and phase images (24–27), but further spurred interest in the quantification of magnetic susceptibility *in vivo*. Hence, within the past decade, ground-breaking work has been undertaken to quantify non-invasively magnetic susceptibility distributions with MRI, which is indeed achievable by estimating the magnetic field distribution from MRI phase data, eliminating so-called background field contributions that may result from magnetization induced outside of the imaging field of view (FOV) and converting the field patterns to the underlying magnetic susceptibility distributions [for recent reviews, see, for example, refs. (28–33)].

In the following, we aim to provide a brief overview of the theoretical and technical foundations underlying QSM and STI, as well as a compilation of some of the current methodological and clinical applications of QSM. As several of the topics on which we touch in our review are covered specifically in greater detail in this special issue, the presentation will be short and concise to provide a more general summary of salient features.

FOUNDATIONS OF QSM

Magnetic susceptibility is a material property that describes the degree of magnetization of a material when placed into an external magnetic field. For isotropic, non-ferromagnetic materials, the magnetic volume susceptibility χ is defined by the linear relation

$$\vec{M} = \chi \cdot \vec{H} \quad [1]$$

where \vec{M} is the magnetization or magnetic dipole moment per unit volume, \vec{H} is the applied magnetic field intensity and χ is a scalar quantity. In free space, where there is no magnetization, the magnetic field can be described equally well by the vector fields \vec{B} or \vec{H} , which are linearly related by $\vec{B} = \mu_0 \cdot \vec{H}$, and thus

scaled versions of each other. In magnetized matter, the magnetic induction or magnetic flux density \vec{B} and the field \vec{H} are related by:

$$\begin{aligned} \vec{B} &= \mu_0 \cdot (\vec{H} + \vec{M}) \\ &= \mu_0 \cdot (1 + \chi) \cdot \vec{H} \end{aligned} \quad [2]$$

where μ_0 is the magnetic permeability of free space. As both \vec{M} and \vec{H} have the same units (A/m), the volume magnetic susceptibility is dimensionless.

Magnetic susceptibility is a bulk property and does not describe the detailed response of matter to an external field on a microscopic or molecular scale, but rather describes the response derived from mean fields averaged over many molecules. In anisotropic materials or specific biological tissue constituents, such as lipid bilayers, proteins, muscle fibers or white matter (WM) fiber bundles, susceptibility becomes orientation dependent with respect to an external magnetic field, and is then described by a symmetric second rank tensor (34–38) from which tensor parameters, such as the mean magnetic susceptibility $[\bar{\chi} = (\chi_{11} + \chi_{22} + \chi_{33})/3]$ or axial magnetic susceptibility anisotropy $[\chi_{aa} = \chi_{11} - (\chi_{22} + \chi_{33})/2 = \chi_{\parallel} - \chi_{\perp}]$, can be extracted [χ_{11} , χ_{22} and χ_{33} are the eigenvalues of the susceptibility tensor ordered from large to small; $\chi_{\parallel} = \chi_{11}$ and $\chi_{\perp} = (\chi_{22} + \chi_{33})/2$].

On a microscopic scale, the magnetization of a sample is far from being a smooth vector function. Indeed, seen from the viewpoint of nuclear spins (protons), which can be considered as magnetic dipole sources with negligible spatial extent, microscopically the magnetization in the sample appears to fluctuate strongly, which needs to be considered when trying to make a connection between the atomic structure of matter and a macroscopic description of electromagnetic phenomena. Referring to the work of Lorentz (39), who first developed a theory of this type, and considering the extensive randomization that takes place in the nuclear spin system as a result of time averaging, diffusion averaging and averaging over nuclei, allows one to treat the average magnetic environment of a proton as an approximate continuum apart from a dedicated exclusion volume surrounding the proton (40). The latter can be described by the Lorentz sphere, which is a fictitious construct that serves to separate near-field contributions and far-field contributions to facilitate the calculation of the magnetic field acting at the site of a nucleus (29). Magnetic moments inside the Lorentz sphere are dealt with individually, whereas those located outside are accounted for by continuum theory. By considering further the demagnetization field which is induced in the sample when placing it into a magnetic field, and which depends on the sample's susceptibility, shape, internal structure and orientation, makes it possible to determine the total local field at the site of the nucleus of interest by summing all of these field contributions. [For a recent comprehensive review, which is related, amongst others, to these issues, see ref. (29).] Interestingly, in homogeneous spherical samples, the local field is identical to the applied external field, whereas, in spheroidal samples, a constant field offset results, which depends on the shape and orientation of the sample. In non-spheroidal samples, the demagnetization fields are inhomogeneous and lead to spatially dependent modifications of the local precession

frequencies (41). Demagnetization fields, which have their origin in the magnetization of the sample, can be effectively described via the introduction of the demagnetization tensor, which is a purely geometrical function that depends only on the shape of the sample. In the case of spheroids, the three eigenvalues of the demagnetization tensor (also called demagnetizing factors) are position independent; in the case of spherical samples, the demagnetization tensor becomes a single scalar of the numerical value 1/3.

Bearing in mind these remarks and the necessary local field correction outlined above, we proceed to consider the contribution made to the macroscopic magnetic induction field by a magnetized object, whose magnetization $\vec{M}(\vec{r})$ at every point \vec{r} within the object is known, by introducing the vector potential $\vec{A}(\vec{r})$ (42):

$$\vec{A}(\vec{r}) = \frac{\mu_0}{4\pi} \iiint \frac{\vec{M}(\vec{r}') \times (\vec{r} - \vec{r}')}{|\vec{r} - \vec{r}'|^3} d^3\vec{r}' \quad [3]$$

The field variation $\Delta\vec{B}(\vec{r})$ due to the source of $\vec{M}(\vec{r})$ is obtained by taking the curl of the vector potential:

$$\Delta\vec{B}(\vec{r}) = \frac{\mu_0}{4\pi} \iiint \nabla \times \left[\frac{\vec{M}(\vec{r}') \times (\vec{r} - \vec{r}')}{|\vec{r} - \vec{r}'|^3} \right] d^3\vec{r}' \quad [4]$$

Using the vector identity $[\vec{\nabla} \times (\vec{A} \times \vec{B}) = \vec{A} \cdot \vec{\nabla} \cdot \vec{B} - \vec{B} \cdot \vec{\nabla} \cdot \vec{A} + (\vec{B} \cdot \vec{\nabla}) \vec{A} - (\vec{A} \cdot \vec{\nabla}) \vec{B}]$ and noting that the *del* operator operates on (\vec{r}) then yields:

$$\Delta\vec{B}(\vec{r}) = \frac{\mu_0}{4\pi} \iiint \left[\frac{3\vec{M}(\vec{r}') \cdot (\vec{r} - \vec{r}')}{|\vec{r} - \vec{r}'|^5} \cdot (\vec{r} - \vec{r}') - \frac{\vec{M}(\vec{r}')}{|\vec{r} - \vec{r}'|^3} \right] d^3\vec{r}' \quad [5]$$

Assuming that the main field $\vec{B}_0 = [0 \ 0 \ B_0]^T$ is oriented in the z direction, we may simplify Equation [5] by considering only the z-components of the corresponding vector quantities, which leads to:

$$\Delta B_z(\vec{r}) \approx \frac{\mu_0}{4\pi} \iiint \left[\frac{3M_z(\vec{r}') \cdot (z - z')}{|\vec{r} - \vec{r}'|^5} \cdot (z - z') - \frac{M_z(\vec{r}')}{|\vec{r} - \vec{r}'|^3} \right] d^3\vec{r}' \quad [6]$$

Closer inspection of Equation [6] implies that this equation can be written as a convolution between $M_z(\vec{r})$ and the z-component of the point-dipole response (or Green's function) $d_z(\vec{r})$ (43–45):

$$\Delta B_z(\vec{r}) = \mu_0 \cdot \int M_z(\vec{r}') \cdot d_z(\vec{r} - \vec{r}') d^3\vec{r}' \quad [7]$$

where:

$$d_z(\vec{r}) = \frac{1}{4\pi} \cdot \frac{3 \cos^2(\theta) - 1}{|\vec{r}|^3} = \mathcal{F}^{-1} \left\{ \frac{1}{3} - \frac{k_z^2}{|\vec{k}|^2} \right\} \quad [8]$$

The vector quantities \vec{r} and \vec{k} are the coordinate positions in image space and *k*-space, respectively, and \mathcal{F}^{-1} denotes the inverse Fourier transform. θ is the angle between the z direction and \vec{r} . With the condition $|\chi| \ll 1$, the approximation $M_z(\vec{r}) \approx \chi(\vec{r}) \cdot \mu_0^{-1} \cdot B_0$ in Equation [7] then provides the link between the magnetic field variations that are induced by the susceptibility distribution, which can also be written in the following form:

$$\begin{aligned} \Delta B_z(\vec{r}) &= B_0 \cdot \int \chi(\vec{r}') \cdot d_z(\vec{r} - \vec{r}') d^3\vec{r}' \\ &= \mathcal{F}^{-1} \left\{ \chi(\vec{k}) \cdot d_z(\vec{k}) \right\} \cdot B_0 \end{aligned} \quad [9]$$

where $\chi(\vec{k})$ denotes the Fourier transform of $\chi(\vec{r})$. The challenge now is to determine $\Delta B_z(\vec{r})$ from MR measurements and solve the inverse problem as expressed in Equation [9] to determine the susceptibility distribution on a pixel-by-pixel basis.

As the local magnetic field $[B(\vec{r}) = B_0 + \Delta B_z(\vec{r})]$ at the site of a nucleus determines the Larmor frequency of that nucleus:

$$f_L(\vec{r}) = \gamma [B_0 + \Delta B_z(\vec{r})] \quad [10]$$

where γ is the gyromagnetic ratio (γ) divided by 2π , Equation [10] provides the basis to determine the magnetization-induced magnetic field variations. This becomes more obvious when considering the measured frequency variation $\Delta f(\vec{r})$ between the local resonance frequency (f_L) and the scanner's reference frequency $f_R \approx \gamma B_0$:

$$\begin{aligned} \Delta f(\vec{r}) &= f_L(\vec{r}) - f_R \\ &= \gamma \Delta B_z(\vec{r}) \end{aligned} \quad [11]$$

Consequently, any MR sequence accruing phase during the data acquisition window in proportion to $\Delta B_z(\vec{r})$ can be utilized, in principle, to monitor field variations. What we neglect here are contributions to the local resonance frequency caused by chemical shift effects, which depend on the specific molecular environment of the nucleus (40). In brain imaging, chemical shifts may be neglected to first approximation, but they become important and must be accounted for in tissues containing larger fractions of fat, such as in abdominal tissue. Likewise, effects caused by exchange between water protons and protons of macromolecules are not considered (46–48).

MRI DATA ACQUISITION FOR QSM

GRE sequences are particularly suited in this respect, as their associated phase maps $[\phi(\vec{r})]$ or, equivalently, frequency maps $[\Delta f(\vec{r})]$ reflect the sample magnetization and thus its magnetic

susceptibility. The GRE signal phase $\phi(\vec{r}, TE)$ at echo time, TE, can be written as (49):

$$\begin{aligned}\phi(\vec{r}, TE) &= \phi_0(\vec{r}) + 2\pi \cdot \Delta f(\vec{r}) \cdot TE \\ &= \phi_0(\vec{r}) + \gamma \cdot \Delta B_z(\vec{r}) \cdot TE\end{aligned}\quad (12)$$

where $\phi_0(\vec{r})$ is a coil sensitivity-dependent phase offset originating from the radiofrequency response of the sample. With TE strongly influencing the sensitivity of GRE phase images to magnetic field perturbations, whilst, at the same time, deteriorating the phase signal-to-noise ratio (SNR), it has been shown that optimum phase contrast is achieved for a TE equal to the tissue's effective transverse relaxation time T_2^* (24). However, as, usually, a variety of tissue types with different T_2^* values are collected by MRI *in vivo*, a single-echo acquisition cannot reflect the magnetic field variation across all tissues in an optimal manner. Hence, the use of multi-echo GRE sequences has been suggested for QSM, as it offers more flexibility in tailoring the contrast caused by susceptibility effects and allows the calculation of the effective transverse relaxation rate (R_2^*), as well as the determination of magnetic field perturbations with higher SNR (50,51). For instance, Wu *et al.* (50) combined frequency maps obtained at different TEs by taking into account the local TE-dependent contrast-to-noise ratio (CNR) of the individual frequency maps to achieve a more than two-fold increase in SNR when using 11 GREs compared with single-echo imaging. Furthermore, with multi-echo GRE imaging, temporal phase evolution can be analyzed, which helps to identify voxels with reliable phase values.

Sequence variants with and without flow compensation are currently in use. It is, however, advisable to apply flow compensation in all three spatial directions to overcome blood flow-induced phase shifts (52–54), because such phase shifts cannot be explained by magnetic susceptibility and may then result in non-local artifacts occurring adjacent to arterial vessels with high blood flow on the susceptibility maps. Remnant, flow-induced phase shifts may also affect magnetic susceptibility values extracted from venous vessels.

One important issue concerns the choice of the imaging resolution, as this will affect the accuracy of the estimated susceptibilities. Unfortunately, there is no single answer to this question, as the optimal resolution depends on the size of the investigated object or the details of the object in which one is interested. There is a trade-off between the use of higher spatial resolution with its concomitant reduction in partial volume effects (particularly for smaller structures) and thus improved accuracy in susceptibility estimation, on the one hand, and the prolonged acquisition time with decreased SNR and increased uncertainties of phase that translate into errors of the reconstructed susceptibility values, on the other. Haacke *et al.* (33) have recently provided rather comprehensive recommendations for the choice of suitable imaging parameters at field strengths of 1.5T, 3T and 7T. From these recommendations and focusing on clinical neuroimaging at 1.5T and 3T, it follows that spatial resolutions of about $0.5 \text{ mm} \times 0.5 \text{ mm} \times 2 \text{ mm}$ represent a reasonable compromise between acceptable accuracy and acquisition time.

GRE scan times may be shortened – albeit at the expense of potentially higher noise levels – by employing dedicated phased-array coils, sophisticated *k*-space sampling and/or

reconstruction techniques compared with conventional Cartesian sampling. Tissue features and contrast are well maintained in frequency maps reconstructed from under-sampled datasets, but suffer from higher noise levels (50). Fast imaging readouts, including two-dimensional echo planar imaging (EPI) (55), three-dimensional EPI (56), spiral imaging (50) or traversing *k*-space with a corkscrew trajectory [wave-CAIPI (controlled aliasing in parallel imaging)] (57), have been implemented to acquire data for QSM reconstruction. Bilgic *et al.* (58) were recently able to speed up three-dimensional GRE imaging with wave-CAIPI by acceleration factors up to 15, and collected whole head data with 1.1 mm isotropic resolution within 90 s at 3 T.

Alternative acquisition methods to collect frequency variations include water saturation shift referencing (WASSR) (59), asymmetric spin echo imaging or balanced steady-state free precession (bSSFP) MRI (60).

COMPUTATIONAL STRATEGIES FOR DETERMINATION OF MAGNETIC SUSCEPTIBILITY

In this section, we briefly focus on several steps needed to process GRE phase images and introduce techniques for solving the ill-posed inverse problem of the determination of the magnetic susceptibility. The pipelines for data processing of single orientation acquisitions (as typically used for QSM) and multiple orientation acquisitions (as required for STI) are summarized schematically in Fig. 1.

Coil combination

Phased-array coils are typically employed for MR signal reception and require the composition of images from each coil channel into a single combined image. Some combination methods [e.g. ref. (61)] suffer from the occurrence of open-ended fringe lines (singularities) in the resulting phase image, which impede accurate susceptibility quantification. Other methods apply a high-pass filter to remove the channel-dependent phase offsets prior to complex image summation (62,63) which, however, are also not suited for QSM or STI, because slowly varying phase contributions are thereby suppressed which may, indeed, reflect certain tissue structures (e.g. the globus pallidus in brain measurements) (64). A suitable approach is to combine the complex single-channel images by taking the argument of the complex summed single-channel images after having subtracted the channel-dependent phase offset (offset-corrected phase combination method) (27,65,66). This phase offset may be determined as a constant for each channel from a region of interest placed in the center of the imaged object (27,65,67), or as a spatial map by exploiting the temporal phase evolution of multi-echo acquisitions (66). The latter method is preferred, especially at ultra-high magnetic field strengths ($B_0 \geq 7 \text{ T}$) to overcome potentially occurring SNR reductions in some regions.

Alternatively, calculation of the Hermitian inner product between the complex data of one echo (*m*; e.g. $m = 1$) and that of another echo (*n*; e.g. $n = 2$), summing over all coil channels and finally taking the argument may be applied to create a phase difference image, $\Delta\phi(\vec{r})$, with an effective TE of $TE_n - TE_m$ from all receiver channels (68,69):

$$\Delta\phi(\vec{r}) = \arctan \left[\frac{\sum_{j=1}^{N_c} S_{n,j} S_{m,j}^*}{\sum_{j=1}^{N_c} S_{n,j} S_{m,j}} \right]. \quad [13]$$

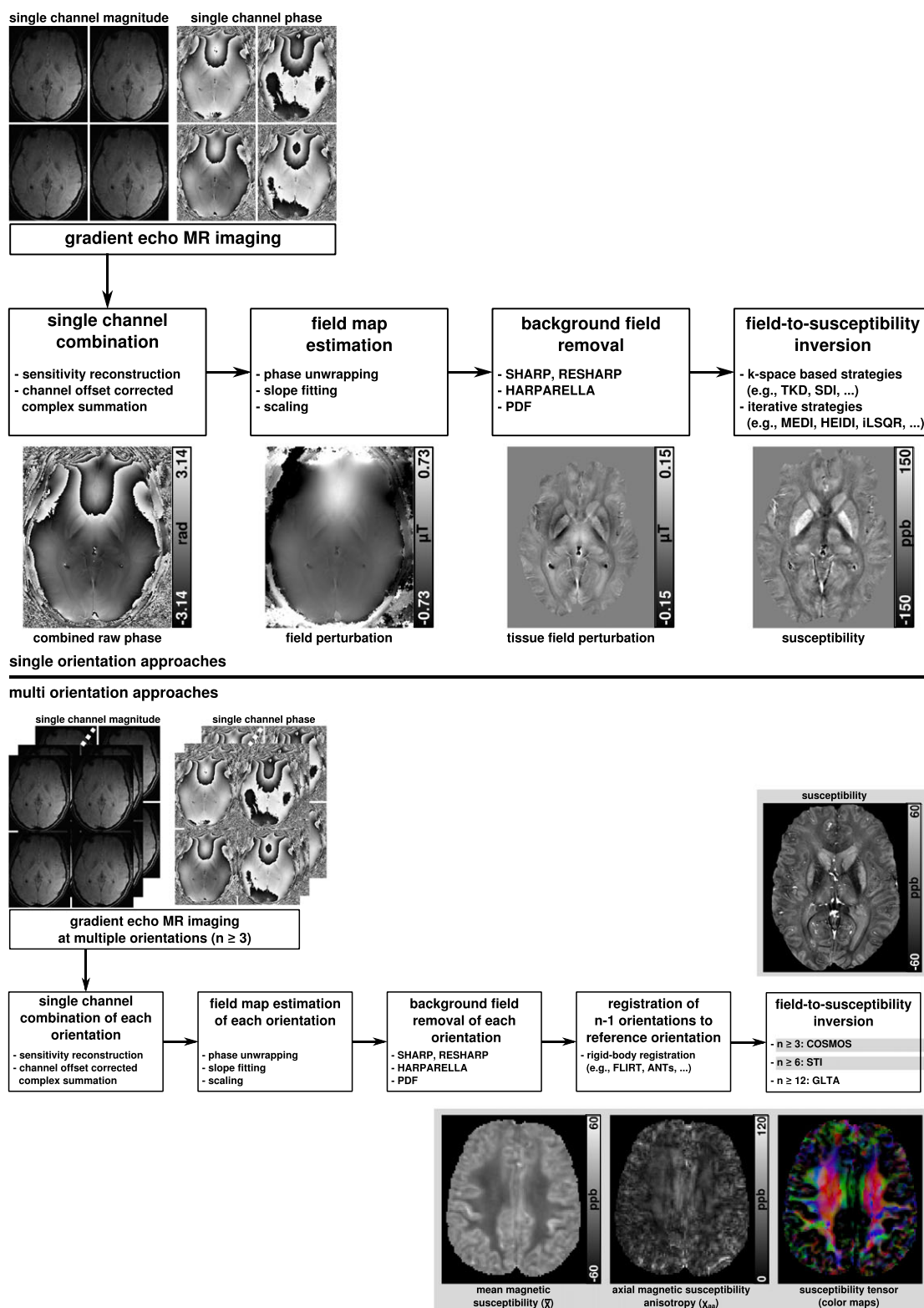


Figure 1. Processing steps to convert gradient echo phase images into magnetic susceptibility for single orientation susceptibility mapping (top row) and multiple orientation susceptibility computation (bottom row). The maps of the mean magnetic susceptibility ($\bar{\chi}$), magnetic susceptibility anisotropy (χ_{aa}) and color-coded principal eigenvectors of the susceptibility tensor, shown in the bottom row, are courtesy of Wei Li (MRI Division, Research Imaging Institute, University of Texas Health Science Center at San Antonio, San Antonio, TX, USA) and Chunlei Liu (Brain Imaging and Analysis Center, Duke University School of Medicine, Durham, NC, USA). ANTs, advanced normalization tools; COSMOS, calculation of susceptibility through multiple orientation sampling; FLIRT, FMRIB's linear image registration tool; GLTA, generalized Lorentzian tensor approach; HEIDI, homogeneity-enabled incremental dipole inversion; HARPARELLA, harmonic (background) phase removal using the laplacian operator; MEDI, morphological-enabled dipole inversion; PDF, projection onto dipole fields; RESHARP, regularization enabled SHARP; STI, susceptibility tensor imaging; SHARP, sophisticated harmonic artifact reduction for phase data; TKD, thresholded k -space division.

N_c is the number of channels and * denotes the complex conjugate of S_m . Here, the channel-dependent phase offsets are removed by calculating the phase differences. As both methods, the offset-corrected phase combination and phase difference methods, enable the combination of phase images without an exact knowledge of the complex-valued coil sensitivity, they are well suited for ultra-high-field imaging, where coil sensitivity data are not easily available because of the lack of a volume body coil (70). If a body coil is part of the MR scanner, uniform sensitivity reconstruction (SENSE) can be used whilst taking into account the object-specific complex-valued coil sensitivities to combine the complex data with optimal SNR (71–73). More recent work has also suggested multi-channel data combination using linear phase baseline correction (74) or improved adaptive reconstruction (75).

Magnetic field mapping

As MRI detects phase values only within a range of $[-\pi, \pi)$ rather than the full phase evolution of the magnetization, aliasing may occur if the phase exceeds $|\pi|$. Phase aliasing results in abrupt artificial jumps of 2π , so-called phase wraps (see the combined raw phase image in the top row of Fig. 1), and the wrapped phase $\phi_w(\vec{r})$ is consequently different from the true phase evolution. To estimate the true phase $\phi(\vec{r})$, wraps must be compensated for by locally adding multiples of 2π (76):

$$\phi(\vec{r}) = \phi_w(\vec{r}) + n(\vec{r}) \cdot 2\pi \quad [14]$$

The correct integer number $n(\vec{r})$ may be determined by analyzing the temporal phase evolution (77,78) or the spatial phase distribution (79–82). In the spatial domain, phase unwrapping strategies mainly rely on one of the following techniques: path following (i.e. the unwrapping process starts from a grid point and follows a discrete spatial unwrapping path) (79–81); minimum norm solving (i.e. the phase unwrapping problem is formulated as the minimization of the difference between the wrapped phase differences and the unwrapped phase differences in a generic L_p -norm sense) (76); or filtering (i.e. phase unwrapping is featured with filtering the phase noise and unwrapping the phase simultaneously) (83,84). Schofield and Zhu (82) proposed a path-independent algorithm, usually denoted as Laplacian-based phase unwrapping, that relies on solving partial differential equations and calculating derivatives using fast Fourier transforms. As a result of its numerical simplicity and its ability to unwrap noisy phase maps, this algorithm is frequently used in QSM. With multi-echo data, spatial domain unwrapping is typically applied on an echo-by-echo basis and phase aliasing between the corrected volumes is solved by applying an additional temporal unwrapping. Irregular echo spacing may be adjusted in multi-echo GRE imaging to facilitate unwrapping of highly wrapped images (78).

The magnetic field perturbation $\Delta B_z(\vec{r})$ may then be obtained by dividing the unwrapped phase images by the term $\gamma \cdot TE$ and properly taking into account the phase offset in Equation [12]. An elegant way to disentangle transmit-related and static field perturbation-related phase contributions is to exploit the approximately linear relationship between phase and TE in multi-echo GRE experiments by voxel-wise fitting of

the unwrapped phase images. In the case of single-echo data, its contribution can be suppressed in some of the reported background field removal approaches by incorporating, for instance, regularization.

Background field removal

MR information is, in general, obtained from a region of an object determined by the FOV, and is only available in the presence of a sufficiently high proton density of mobile hydrogen protons. The magnetic field perturbation within a given volume of interest (VOI), such as the human brain, is, however, additionally influenced by the magnetic susceptibility distribution outside that VOI (e.g. skull, paranasal sinus, human torso), which is also exposed to the static magnetic field of the scanner, as well as by contributions caused by main field inhomogeneities and shimming fields. Consequently, the number of source samples contributing to the field perturbation (and thus the phase or frequency maps) in the VOI largely exceeds the number of available phase data samples in the VOI, rendering the field-to-susceptibility problem in Equation [9] highly under-determined.

To overcome this problem, one possible solution is to reduce the number of unknowns in the field-to-susceptibility inversion procedure by decomposing the estimated magnetic field perturbation $\Delta B_z(\vec{r})$ into field contributions generated by the susceptibility distribution within the VOI $[\Delta B_{int}(\vec{r})]$ and outside the VOI $[\Delta B_{bkg}]$ (44,64,85):

$$\Delta B_z(\vec{r}) = \Delta B_{int}(\vec{r}) + \Delta B_{bkg}(\vec{r}) \quad [15]$$

and to restrict the inversion to the VOI. As the background field contributions are usually about an order of magnitude stronger than the internal field contributions, efficient strategies for removing the background field variations need to be applied prior to solving Equation [9].

Several approaches have been developed to separate background and internal (tissue) fields, including: (i) solving the Laplacian equation by utilizing the spherical mean value property of the background field, which is referred to as the sophisticated harmonic artifact reduction for phase data (SHARP) method (64,85–87); (ii) projecting the total magnetic field to the dipole fields generated by the magnetization outside the VOI, which is referred to as the projection onto dipole fields (PDF) method (88,89); and (iii) solving the Laplacian equation by assuming a boundary value, which is referred to as the Laplacian boundary value method (90).

The PDF method fits a hypothetical distribution of susceptibility values outside the VOI to reproduce the background field within the VOI (88,89,91). The SHARP method convolves $\Delta B_z(\vec{r})$ with a radial kernel, followed by the removal of convolution edge artifacts by masking, and deconvolution. The last step usually applies regularization using truncated singular value decomposition (64,92) or Tikhonov regularization (93). Both PDF and SHARP derivatives share the limitation that the background field close to the boundary of the VOI cannot be extracted accurately because the orthogonality assumption between dipole fields originating outside and inside the VOI breaks down in the case of PDF, and convolution edge artifacts occur during SHARP processing. Several strategies for reducing boundary

problems in the SHARP approach have been proposed, including the computation of the background field by differently sized radial kernels (87,94), utilization of the Laplacian as the convolution kernel (86,90,92,95) or propagating the background field using Taylor series expansion (96). One remaining challenge concerns the possibility that the non-local magnetic field induced by one tissue (e.g. putamen) can affect neighboring tissue (e.g. WM adjacent to the putamen) and act as a small background field there. Such a situation is not disentangled by current background phase removal techniques, resulting in a spatially non-local representation of tissue structures on background-corrected field maps.

Another background field removal alternative is the geometry-dependent artifact correction approach (97), in which the geometry of the air–tissue interfaces is determined based on additionally acquired three-dimensional T_1 -weighted GRE magnitude images, and the background field induced by these air–tissue interfaces is predicted through a fast forward calculation. This method is found to be effective in reducing the background field, but the accuracy depends on the correctness of the extracted geometries.

Finally, the resulting relationship between the background field-corrected magnetic field perturbation map $\Delta B_{\text{int}}(\vec{r})$ and the magnetic susceptibility distribution can then be written as:

$$\Delta B_{\text{int}}(\vec{r}) = B_0 \cdot \int_{\text{VOI}} \chi(\vec{r}') \cdot d_z(\vec{r} - \vec{r}') d^3 \vec{r}' \quad [16]$$

From tissue magnetic field perturbation to bulk magnetic susceptibility

Equation [16] implies that the bulk magnetic susceptibility distribution in the VOI can be determined by deconvolving $\Delta B_{\text{int}}(\vec{r})$ with the point-dipole response $[d_z(\vec{r})]$. However, in order to do

so, the integration limits of the integral in Equation [16] and thus the definition of $\chi(\vec{r})$ must be extended to infinity. Rewriting Equation [16]:

$$\begin{aligned} \Delta B_{\text{int}}(\vec{r}) &= B_0 \cdot \int_{-\infty}^{\infty} u(\vec{r}') \cdot \chi(\vec{r}') \cdot d_z(\vec{r} - \vec{r}') d^3 \vec{r}' \\ &= B_0 \cdot \int_{-\infty}^{\infty} \tilde{\chi}(\vec{r}') \cdot d_z(\vec{r} - \vec{r}') d^3 \vec{r}' \end{aligned} \quad [17]$$

where $\tilde{\chi}(\vec{r}) = u(\vec{r}) \cdot \chi(\vec{r})$ and $u(\vec{r})$ denotes a function whose value is unity inside and zero outside the VOI, then allows us to formulate the deconvolution (\otimes^{-1}) as:

$$\begin{aligned} \tilde{\chi}(\vec{r}) &= (\Delta B_{\text{int}}(\vec{r}) \otimes^{-1} d_z(\vec{r})) \cdot B_0^{-1} \\ &= \mathcal{F}^{-1} \left\{ \frac{\mathcal{F} \{ \Delta B_{\text{int}}(\vec{r}) \}}{\mathcal{F} \{ d_z(\vec{r}) \}} \right\} \cdot B_0^{-1} \end{aligned} \quad [18]$$

which gives the magnetic susceptibility $\tilde{\chi}(\vec{r})$ inside the VOI under the constraint of a constant value outside the VOI (29). However, direct evaluation of Equation [18] is not possible because the point-dipole response in the Fourier domain [Equation [8]] contains zeros on two conic surfaces at the magic angle ($\theta \approx 54.7^\circ$) and small values in the direct vicinity of the magic angle cones, rendering the inverse problem of QSM ill-posed, meaning that there exist multiple mathematical susceptibility distributions corresponding to the same measured field. Consequently, even small noise contributions in the field map are substantially amplified in k -space regions close to these conic surfaces, causing severe streaking artifacts in the reconstructed susceptibility maps (Fig. 2A, D) (98).

Several methods to overcome the ill-posed nature of the inverse problem have been developed, which basically rely either on repeated measurements of the object after having

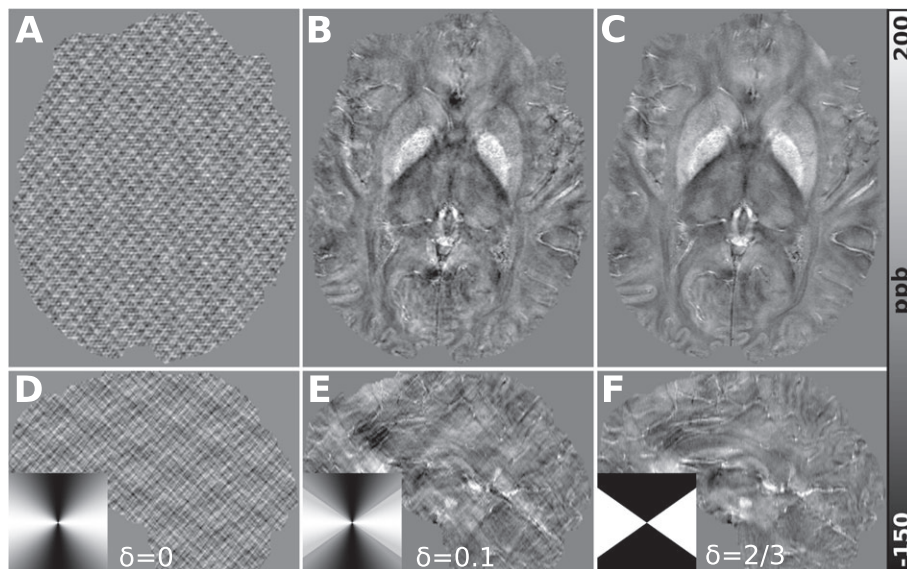


Figure 2. Transverse (A–C) and sagittal (D–F) views of susceptibility maps generated with thresholded k -space division (TKD) using different thresholds (δ). Severe artifacts and noise amplification are observed with direct inversion of the original dipole kernel (A, D). Inversion with a kernel using $\delta = 0.1$ (B, E) substantially reduces artifacts, but streaking artifacts are still discernible, in particular in the sagittal view (E). TKD with a threshold of 2/3 successfully removes the streaking artifacts (C, F). The corresponding Fourier domain dipole function $[d_z(\delta, \vec{k})]$ is depicted as an inset in the images in the bottom row and the signal intensity range is adjusted between $-2/3$ and $1/3$.

been rotated with respect to the magnetic field or on the utilization of regularization.

Computation of magnetic susceptibility based on multiple measurements

One approach to compute magnetic susceptibility maps (although clinically not applicable because of severe discomfort to subjects) is to acquire multiple MRI measurements with different orientations of the object (e.g. human head) to the main magnetic field. This method has been denoted as 'calculation of susceptibility through multiple orientation sampling' (COSMOS) (45,64,91,99,100) and exploits the fact that the orientation of the magic angle cone regions follows the object rotation relative to the magnetic field. With three or more independent object orientations, the zero cone surfaces of the Fourier domain kernels do not intercept and all Fourier coefficients can be determined (91,99), which enables the computation of the magnetic susceptibility distribution without priors and regularization by solving simultaneously the now over-determined field-to-susceptibility problem. As the resulting susceptibility maps exhibit excellent quality with virtually no streaking artifacts, COSMOS has often been considered as the gold standard of QSM, in particular when tailoring regularization strategies of single-orientation QSM algorithms or visualizing the cerebral anatomy in detail. It should, however, be noted that COSMOS is also expected to average contributions owing to sources other than isotropic susceptibility (101), and that the effects of microstructural anisotropy and/or anisotropic magnetic susceptibility on maps reconstructed with COSMOS must be investigated further in future studies.

Computation of magnetic susceptibility based on single measurements

A variety of methods have been introduced to determine the magnetic susceptibility distribution based on a single MRI acquisition by incorporating regularization. These methods may be broadly divided into three groups: the first group comprises non-iterative k -space techniques, and the second and third groups include iterative image space-based optimization approaches that apply regularization to either all Fourier coefficients or only to Fourier coefficients close to the magic angle cone, respectively.

A time-efficient QSM technique belonging to the first group is to solve Equation [18] in the Fourier domain by applying a modified dipole kernel $[d'_z(\delta; \vec{k})]$ in which small absolute values are replaced by a constant value (91,95,98):

$$d'_z(\delta; \vec{k}) = \begin{cases} \frac{1}{3} - \frac{k_z}{|\vec{k}|^2} & \text{if } \left| \frac{1}{3} - \frac{k_z}{|\vec{k}|^2} \right| > \delta \\ \text{sign} \left(\frac{1}{3} - \frac{k_z}{|\vec{k}|^2} \right) \cdot \delta & \text{otherwise} \end{cases} \quad [19]$$

Here, 'sign' represents the sign function. This approach, typically referred to as thresholded k -space division (TKD), is appealing because of its numerical simplicity, and has been shown to effectively limit noise amplification in the vicinity of the magic

angle cones. Shmueli *et al.* (98) reported that parameter values of δ in the range 0.2–0.5 effectively reduce both streaking artifacts and noise amplification (Fig. 2), but that systematic underestimation of magnetic susceptibility values occurs with increasing δ . The latter can be explained by the systematic inversion error in the subdomain of the Fourier space, where the dipole kernel has been modified, and can be overcome by introducing a scalar correction factor $c_\chi(\delta)$ depending on the chosen threshold (95):

$$\tilde{\chi}(\vec{r}) = \mathcal{F}^{-1} \left\{ \frac{\mathcal{F} \{ \Delta B_{int}(\vec{r}) \}}{d'_z(\delta; \vec{k}) \cdot c_\chi(\delta)} \right\} \cdot B_0^{-1} \quad [20]$$

The major limitation of TKD is that it applies a generic regularization and that unreliable voxels, whose phase shift is not caused by magnetic susceptibility, cannot be excluded beforehand, potentially creating non-local artifacts in the resulting susceptibility maps (see circle-ended arrow in Fig. 3). Recently, it has been shown that it is possible to impose smoothness to the reconstructed susceptibility map in a direct inversion approach (102,103).

Algorithms of the second group solve the inverse problem in image space using iterative methods, such as steepest descent (SD) or conjugate gradient (CG). To this end, the Euclidean norm (L2 norm) of the difference between the measured magnetic field and the one generated by the convolution of the dipole response and the magnetic susceptibility distribution is minimized:

$$\tilde{\chi}(\vec{r}) = \arg \min_{\tilde{\chi}} \|w \left(\left(\frac{\Delta B_{int}}{B_0} \right) - d_z \otimes \tilde{\chi} \right)\|_2^2 + \lambda \cdot R(\tilde{\chi}) \quad [21]$$

where w is a diagonal weighting function to account for spatially varying noise levels, λ is a tunable regularization parameter and $R(\tilde{\chi})$ describes a functional of the susceptibility map (constraint term) to impose prior knowledge onto the solution (31).

Prior information may be derived from magnitude and phase maps by assuming that they have similar edges to the underlying brain structure or by assuming that natural images are sparse in some basis set. A good overview of the wide range of different regularization forms has been provided recently by Wang and Liu (31), who classified them into those that impose piece-wise constant susceptibility (18,104), smooth susceptibility or susceptibility gradients (102,105), sparse susceptibility gradients (106) or morphological consistency with the susceptibility map (89,107). For instance, morphological-enabled dipole inversion (MEDI) (107), a widely used inversion technique, presumes that edges in the susceptibility map coincide with edges in the corresponding magnitude images, and imposes this anatomical prior using L1 regularization to the complete Fourier spectrum of the sought after susceptibility distribution. The underlying assumption when incorporating prior edge information from magnitude images is that tissue compartments of reasonably uniform intensities in the magnitude image most probably represent tissues or substances with uniform susceptibility. As the edges in the magnitude image, however, do not necessarily match the anatomical susceptibility boundaries, the employment of magnitude edge priors may introduce some artificial susceptibility values (100,108).

The third algorithm group comprises strategies that use prior knowledge or sparsity constraints (L1 or TV norm) to restore only

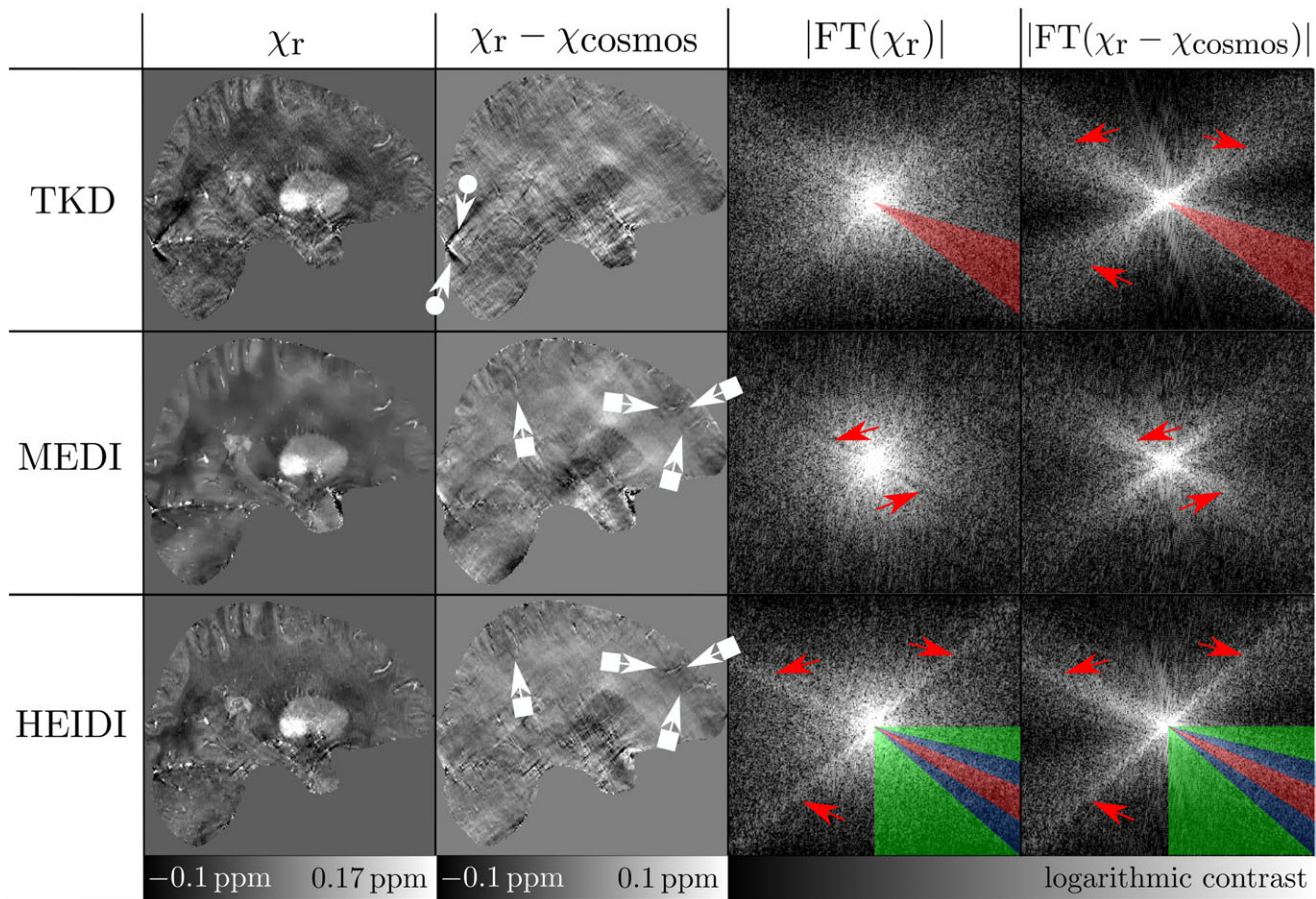


Figure 3. Comparison between quantitative susceptibility mapping (QSM) algorithms. Sagittal slices of the reconstructed susceptibility (χ_r) maps are shown in the first column, the differences with respect to the COSMOS (calculation of susceptibility through multiple orientation sampling) susceptibility (χ_{cosmos}) are depicted in the second column, and the corresponding Fourier spectra are illustrated in the third and fourth columns, respectively. Images computed using thresholded k -space division (TKD), morphological-enabled dipole inversion (MEDI) and homogeneity-enabled incremental dipole inversion (HEIDI) are shown in the rows from top to bottom. Arrows mark subtle underestimations of susceptibility in the cortex (square-ended arrows) and streaking artifacts (circle-ended arrows). The subdomain in Fourier space modified by thresholding the dipole kernel using $\delta = 0.164$ in the TKD approach is highlighted in red (top row). The ill-conditioned subdomain, transitional subdomain and well-conditioned subdomain considered in the HEIDI approach are colored in red, blue and green, respectively (bottom row). Note that only the bottom right region of the symmetrical conical subdomains is indicated. [The figure was modified from ref. (101) with permission from Elsevier.]

the ill-conditioned Fourier coefficients, whilst trusting the non-affected, remaining Fourier coefficients (94,101,109). Homogeneity-enabled incremental dipole inversion (HEIDI) (101), for instance, is based on an incremental inversion procedure in which the Fourier space is separated into three subdomains (A, B, C): an ill-conditioned (A), well-conditioned (B) and interim (C) region (see Fig. 3, sub-image on the bottom right). This method utilizes a priori information about the homogeneity of the susceptibility distribution in the ill-conditioned subdomain only and incorporates it into the reconstruction of the susceptibility distribution, which is optimized based on the application of a total variation norm. The other subdomains (B and C) are reconstructed with a conventional least-squares QR decomposition (LSQR)-based inversion algorithm (18), whereas Fourier coefficients of subdomain (C) are additionally de-noised in image space. Another efficient approach to solve Equation [18] is to apply a k -space/image domain iterative algorithm (110), where, in each iterative step, data points in the region of the magic angle cone are updated with geometry-dependent information. Tang *et al.* (110) considered the geometry of the veins to force the susceptibility outside the veins to be

zero to reduce the streaking artifacts originating from deoxygenated veins with high susceptibility.

Generally, strategies separating k -space are preferable because the magnetic susceptibility is less influenced by the imposed prior information and should reflect the true distribution more closely. This is supported by Fig. 3 which opposes *in vivo* susceptibility maps calculated with selected inversion algorithms from each algorithm group. Although MEDI shows some deviations in regions with subtle susceptibility variations, such as in cortical regions (square-ended arrows), with respect to the corresponding COSMOS map, which has been chosen as reference here, little anatomical contrast is observed in the difference between images calculated with TKD and HEIDI and COSMOS. Streaking artifacts seen in the TKD map (circle-ended arrows) are not discernible in the difference images of both MEDI and HEIDI. Furthermore, the Fourier spectra of the TKD and HEIDI susceptibility maps exhibit substantially increased coefficients compared with that of the COSMOS map, especially in the vicinity of the magic angle cone (red arrows), whereas the Fourier coefficients calculated for the MEDI map are slightly underestimated.

Care should be exercised, however, if subtle (due to, e.g., normal anatomy or WM lesions in patients with multiple sclerosis) or more severe (due to, e.g., large hemorrhages or calcifications) susceptibility variations are both present. With the latter causing rapid T_2^* signal decay, strong signal dephasing and phase errors may introduce severe artifacts in the reconstructed susceptibility maps that may superpose the smaller susceptibility variations. One way to reduce such artifacts whilst preserving subtle susceptibility variations is to apply multi-echo GRE imaging with subsequent field mapping based on fitting of the temporal phase evolution or voxel-wise field map fusion across multiple echoes, as described previously (50). If only single-echo data with rather long TEs (for instance, from a conventional SWI acquisition) are available, artifacts from strong susceptibility variations can be reduced with a two-level QSM approach (111,112). Thereby, regions with strong susceptibility are determined first and used to simulate their field distribution, which is then subsequently removed from the measured total field map. The remaining field distribution is then used to solve for the weaker susceptibility sources and the result is finally superimposed onto the strong susceptibility distribution.

More recently, QSM reconstruction techniques have been introduced that conflate several of the previously mentioned reconstruction steps (see also Fig. 1) by combining phase unwrapping and background phase removal (95) or by incorporating the Laplacian into the inversion process to compute magnetic susceptibility directly on raw MRI phase images (113,114).

From tissue magnetic field perturbation to susceptibility tensor

So far, magnetic susceptibility has been treated as an isotropic, scalar quantity. Several studies, however, have convincingly demonstrated that specific tissues indeed reveal anisotropic magnetic susceptibility, including WM in the brain (34,35,115–117), myocardial tissue (38) and tubules of the kidney (118). An appropriate description of the dependence on orientation then requires the treatment of magnetic susceptibility as a tensor quantity and the relationship between the object-induced field perturbation and the susceptibility tensor $\bar{\chi}$ must be extended (34):

$$\Delta B_{int}(\vec{r}) = \mathcal{F}^{-1} \left\{ \frac{1}{3} \vec{n} \cdot \mathcal{F} \{ \bar{\chi}(\vec{r}) \} \cdot \vec{B}_0 - (\vec{n} \cdot \vec{k}) \cdot \frac{\vec{k}^T \cdot \mathcal{F} \{ \bar{\chi}(\vec{r}) \} \cdot \vec{B}_0}{|\vec{k}|^2} \right\} \cdot \vec{B}_0^{-1} \quad [22]$$

where \vec{n} is a normal vector in the direction of the applied magnetic field \vec{B}_0 and $\bar{\chi}(\vec{r})$ equals the susceptibility tensor inside the VOI and is constant outside the VOI. As magnetic susceptibility is represented by a symmetric tensor, at least six independent measurements are necessary to unambiguously extract the full tensor $\bar{\chi}$ by inverting the system of linear equations formed by Equation [22].

To make this technique more applicable for the study of magnetic anisotropy in the human brain, regularization of the solution of Equation [22] has been proposed in order to reduce the number of necessary object rotations by assuming cylindrically symmetric susceptibility of fibers (115,116) or by penalizing susceptibility variations in the tensor elements (119).

The susceptibility tensor can be visualized using the same techniques as applied to analyze diffusion tensors derived from diffusion-weighted MRI (120,121). Eigenvalue and eigenvector decomposition of the susceptibility tensor serves to define the three principal susceptibilities ($\chi_{11} \gg \chi_{22} \gg \chi_{33}$), together with the corresponding eigenvectors, where the major eigenvector points in the direction with the highest magnetic susceptibility. The course of anisotropic magnetic susceptibility is traceable by assigning a color-coded scheme to the major eigenvector (Fig. 6, see later), in full analogy with diffusion tensor imaging (DTI) (122). Although the underlying physical mechanisms of DTI and STI are completely different, both techniques agree well in delineating the fiber architecture of the brain (see also Fig. 6) (35,121). Therefore, STI may be an alternative tool for the identification of tissue anisotropy, particularly in tissues with low diffusivity or in fixed tissue, where information on neuronal integrity is hard to extract with DTI methods.

In addition to the existence of anisotropic molecular magnetic susceptibilities, the arrangement of the associated molecules or corresponding basic building blocks into microstructurally or micro-compartmentally organized tissues can lead to biased sampling of the magnetic field on a microscopic scale (123) and orientation-dependent frequency shifts that can be ascribed to microstructural anisotropy being present on a subvoxel scale. Hwang and Wehrli (7), for instance, noticed that the field probability density function induced by trabecular bone varies depending on its orientation with respect to the main magnetic field because of bone's anisotropic structure. The effects of microstructural anisotropy on the NMR resonance frequency have also been seen in red blood cells (124,125), muscle fibers (126) and in orientation-dependent measurements of optic nerves *ex vivo* (127,128). Based on an extensive set of experiments and simulations, Wharton and Bowtell (128) were recently able to disentangle the different contributions to the induced frequency variations caused by the radial anisotropic susceptibility in the myelin sheath and the microstructure of WM. Their simulation results suggest that the frequency contribution of microstructure is more dominant than that caused by bulk effects of anisotropic magnetic susceptibility, which has implications when calculating susceptibility maps. One potential solution could be an extension and generalization of Equation [22]. A corresponding theoretical approach, the so-called generalized Lorentzian tensor approach (GLTA), has been proposed recently (129).

MAGNETIC SOURCES OF BIOLOGICAL TISSUE

Almost all human tissues are diamagnetic and, as stated previously, have susceptibilities in a narrow range of about $\pm 20\%$ from the susceptibility of water (12). The most important biophysical sources determining tissue magnetic susceptibility *in vivo* are water, myelin, iron and calcium.

Calcium in tissues, commonly referred to as calcification, has substantially lower magnetic susceptibility than water (diamagnetic susceptibility source). The susceptibility of hydroxyapatite (Ca^{2+}), for instance, has been measured with NMR to be -14.83 ppm (130).

Apart from a tissue's chemical and molecular composition, its microstructure may also affect substantially the measured local frequency within a voxel, and thus the extracted magnetic susceptibility. Microstructural effects on magnetic susceptibility

can be ascribed to: (i) underlying MRI-invisible tissue microstructures at the cellular and subcellular level, i.e. microstructural anisotropy (123,127,129); and (ii) inherent molecular susceptibility anisotropies (34,35,117). Both contributions play a significant role in susceptibility measurements of highly aligned structures, such as WM fiber bundles, renal tubules or muscle fibers.

Myelin

Myelin, being predominantly present in WM, is a significant contributor to tissue magnetic susceptibility. It is a special membrane structure with a high abundance of lipids (e.g. phospholipids [$\chi = -9.68$ ppm, $\chi_{aa} = -1.13$ ppm (131)], sphingolipids consisting of extremely long acids ranging from C₁₈ stearic acid [$\chi = -10.03$ ppm, $\chi_{aa} = -1.22$ ppm (36)] to C₂₄ lignoceric acid) and proteins (132) which, overall, render myelin more diamagnetic than water. Myelin forms a compact multilayered membrane by wrapping itself tightly around the axon, thus supporting efficient transport of action potentials along the axon. The contribution of myelin to the measured bulk susceptibility and its anisotropy has been shown in a number of studies. Liu *et al.* (133) nicely demonstrated the strong contrast between gray matter (GM) and WM, which disappeared in shiverer mice, a transgenic mouse model characterized by the loss of myelin but remaining intact axonal tracts. Preparing a specific arrangement of post-mortem corpus callosum samples, Lee *et al.* (117) demonstrated a dependence of the MRI resonance frequency on the orientation of brain microstructure relative to the main magnetic field, which was attributed to anisotropic WM susceptibility ($\chi_{\parallel} - \chi_{\perp} = 0.012$ ppm). Independent studies using STI also confirmed anisotropy in major fiber bundles (e.g. posterior limb of the internal capsule, genu of the corpus callosum) with values ranging between 0.004 and 0.043 ppm (35,115,116). Quite recently, the anisotropy of the magnetic susceptibility of WM fiber bundles has been directly demonstrated experimentally to vary between 0.014 and 0.019 ppm by studying and analyzing the torque that tends to orient human spinal cord samples in a magnetic field in a direction that maximizes its magnetization (134).

Iron

Despite the presence of trace amounts of paramagnetic transition metal ions, such as copper, manganese and cobalt, it is the significantly higher abundance of iron that creates a dominant paramagnetic contribution to tissue magnetic susceptibility *in vivo* (12). Iron in tissue is either present as storage iron (non-heme iron), such as ferritin and hemosiderin, or is bound to heme proteins, such as in hemoglobin (heme iron) (12,135). Details on the physiological and pathophysiological role of brain iron are given in refs. (136–138).

Histological studies have revealed that brain iron concentration in deep GM nuclei and cortical areas increases with age, typically with a rapid increase from birth until about 20 years of age (139–141). Thereafter, the increase slows down and, in some brain regions, a distinct plateau is reached at middle age. Similar age trajectories have recently been demonstrated non-invasively using QSM *in vivo* (142,143).

The determination of iron concentration with QSM has recently been validated by several post-mortem experiments in combination with alternative iron determination techniques, including X-ray fluorescence (21), inductively coupled plasma mass spectrometry (19) and Perl's staining (22). Consequently,

QSM promises to be a valuable non-invasive tool for the assessment of iron deposition in deep GM nuclei, and offers an elegant possibility to study iron in various neurological and psychiatric disorders.

One important heme iron complex is hemoglobin, a protein in red blood cells to which either O₂ or CO₂ binds, and which dominantly influences the magnetic susceptibility of blood. Neglecting the slight paramagnetic susceptibility shift of dissolved oxygen in plasma, the volume susceptibility of whole blood may be approximated as (144,145):

$$\chi_b = \text{hct} \cdot (Y \cdot \chi_{oxy} + (1 - Y) \cdot \chi_{deoxy}) + (1 - \text{hct}) \cdot \chi_{plasma} \quad [23]$$

where χ_{oxy} and χ_{deoxy} are the magnetic susceptibilities of fully oxygenated and deoxygenated red blood cells, respectively, χ_{plasma} is the magnetic susceptibility of blood plasma, Y is the fractional oxygen saturation and hct denotes the hematocrit. The susceptibility difference between fully oxygenated blood ($Y = 1$) and blood within a venous vessel, $\Delta\chi_b$, only depends on the hematocrit and oxygen saturation:

$$\Delta\chi_b = \Delta\chi_{do} \cdot \text{hct} \cdot (1 - Y) \quad [24]$$

This enables the non-invasive estimation of Y based on magnetic susceptibility in larger, but also smaller (pial), venous vessels if the spatial resolution is high enough to avoid partial volume effects (146). Normal hematocrit values vary between 40–54 (%vol/vol) and 37–47 (%vol/vol) for males and females, respectively (147). For $\Delta\chi_{do} = \chi_{deoxy} - \chi_{oxy}$, different values exist in the literature, e.g. 2.26 ppm (148), 2.51 ppm (149) and 3.39 ppm (144) (in SI units). Recently, the value of 3.39 ppm has been confirmed with MR susceptometry (150).

POTENTIAL OF MAGNETIC SUSCEPTIBILITY CONTRAST TO SOLVE CLINICAL ISSUES

In clinical MRI, SWI, phase imaging and R_2^* mapping are routinely used to assess selected pathological susceptibility variations by depicting, for instance, abnormal venous vessels, (micro)lesions or abnormal iron content (151,152). Although these methods are mathematically less complex than QSM or STI, allowing easier reconstruction, they only measure magnetic susceptibility indirectly, with resulting inferior sensitivity and specificity in selected clinical cases (152–154) and reduced CNR of deep GM (155). Specifically, as SWI is only qualitative, and not quantitative, R_2^* susceptible to intravoxel spin dephasing in the vicinity of steep phase gradients (156) and phase affected by its non-local relation with the underlying magnetic susceptibility distribution (64,157), QSM represents a rather unique tool because it overcomes several of these limitations and enables, amongst others, the differentiation of iron and calcium deposits and improved characterization of pathological iron and/or myelin variations.

So far, both QSM and STI have mainly been applied to study the susceptibility distribution in the human brain. Both techniques have initially been used to investigate healthy individuals because a knowledge of how healthy tissue is reflected by magnetic susceptibility represents an important step to recognize and identify pathological alterations and to potentially shed light on their pathophysiological causes. Moreover, the potential of QSM to assess pathophysiological variations has

been explored for a number of various diseases. The following sections summarize some of the more recent efforts to transfer magnetic susceptibility mapping into the clinic.

Anatomical imaging of the human brain

Thanks to its high sensitivity to myelin and iron in combination with high spatial resolution and field strength exceptionally detailed views into brain morphology have become possible with QSM. It directly reflects subtle variations in tissue composition that have been found to be consistent with histology (22,64,101,158,159). Cerebral substructures can indeed be identified that are, in part, indiscernible on conventional image contrasts (108,158,159). As an example, Fig. 4 displays a susceptibility map of the basal ganglia at the level of the internal globus pallidus. Most striking is the superb contrast between iron-laden deep GM nuclei and the surrounding tissue. Both the lamina pallidi lateralis (arrow g) and the lamina pallidi incompleta (arrow i) are seen on this map, which divide the globus pallidus into an external (pallidum laterale) part and two internal parts (pallidum mediale externum and pallidum mediale internum). Pallidofugal fibers running from the subthalamic nucleus to the globus pallidus and traversing the internal capsule can be identified as elongated structures with increased magnetic susceptibility compared with their surroundings (160). Thus, QSM carries great potential to improve targeting in deep brain surgery, where high and spatially well-localized contrast is essential (161,162) (see 'Neurosurgical planning' section).

In cortical GM, magnetic susceptibility varies substantially depending on the anatomical location (158,163,164). High magnetic susceptibility has been observed in regions with putative high myelin content, such as the primary motor cortex, primary sensory cortex, auditory cortex and paracentral lobule, which suggests the co-localization of iron and myelin in these areas, an issue that has already been demonstrated in the visual cortex (165).

In the cerebellum, QSM depicts the cerebellar nuclei in great detail and with unprecedented contrast (58,64,108,166), as demonstrated in Fig. 5. Compared with susceptibility-weighted, T_1 -weighted and T_2 -weighted images, delineation with QSM is superior, particularly with respect to the gyrification of the dentate nucleus, thus opening the way to non-invasive investiga-

tions of volume, shape and iron content in diseases involving the cerebellar nuclei, such as degenerative cerebellar ataxia.

As mentioned previously, WM fiber tracts, which are dominated by diamagnetic myelin, exhibit magnetic susceptibility anisotropy that leads to an orientation-dependent appearance on QSM with respect to the main magnetic field. This anisotropy is distinctly better assessed by the application of STI instead of QSM, as the former not only allows the extraction of the tensor parameters $\bar{\chi}$ and χ_{aa} , but also the extraction of the anisotropy direction. As illustrated in Fig. 6, STI provides a clear separation of large fiber bundles that are in close contact, but of different orientation (e.g. corpus callosum and cingulate gyrus), indicating that the orientation of the measured susceptibility tensor is indeed related to WM's micro-architecture (35).

Susceptibility-based lesion classification

Intracerebral lesions occur in multiple varieties, including traumatic brain injuries, ischemia, intracerebral hemorrhages, tumors and metastases, with potentially devastating outcomes (167). Therefore, the identification and assessment of a lesion is crucial in clinical diagnosis, therapy and surgical planning. Unequivocal discrimination between blood products (e.g. hemorrhages, cavernomas) and calcifications is often important and is indeed possible by identifying the magnetic susceptibility (16–18). It has already been confirmed that calcifications identified by QSM coincide with findings on computed tomography (CT) scans (18,28,168), which are considered to be the non-invasive gold standard.

Traumatic brain injury

Traumatic brain injury (TBI) is a heterogeneous pathology that is often associated with (micro)hemorrhages resulting from blood–brain barrier permeability changes and injuries of small vessels, particularly in settings of diffuse axonal injury (169). The presence and location of TBI-related (micro)hemorrhages appear to correlate with specific neuropsychological deficits (170,171). In previous studies, SWI has demonstrated greater accuracy than CT and conventional MRI techniques in the detection of trauma-related (micro)hemorrhages (172–174). However, SWI shows inherent blooming effects that, on the one hand, facilitate

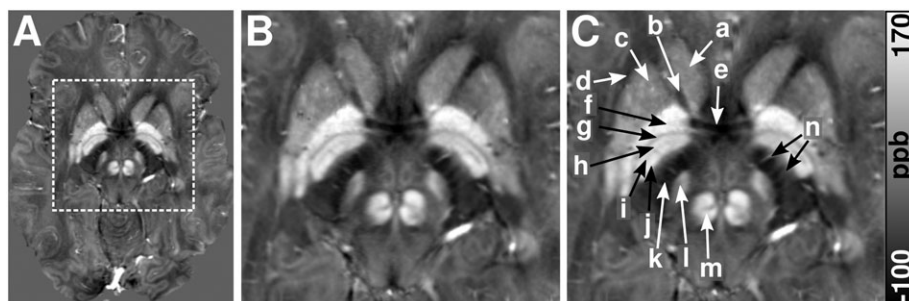


Figure 4. Quantitative susceptibility map showing the basal ganglia of a healthy volunteer. The dashed rectangle on the susceptibility map in (A) indicates the enlarged section in (B) and (C). The susceptibility map clearly reveals: a, head of the caudate nucleus; b, anterior limb of the internal capsule; c, putamen; d, external capsule; e, anterior commissure; f, external globus pallidus; g, lamina pallidi medialis; h, pallidum mediale externum (external segment of the internal globus pallidus); i, lamina pallidi incompleta; j, pallidum mediale internum (internal segment of the internal globus pallidus); k, posterior limb of the internal capsule; l, subthalamic nucleus; m, red nucleus; n, pallidofugal fibers. Brain areas with putatively high iron content (e.g. globus pallidus, subthalamic nuclei, red nuclei) are particularly well discernible. [The figure was modified from ref. (158) with permission from Elsevier.]

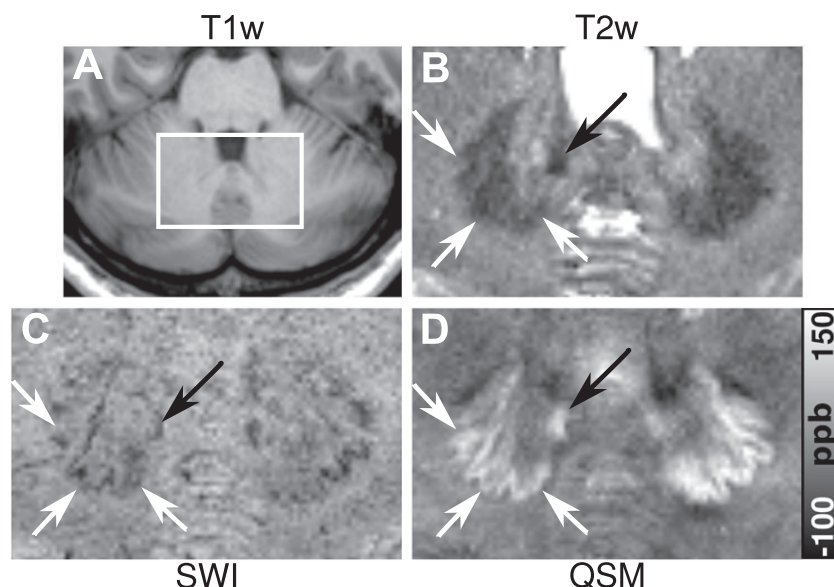


Figure 5. MRI of the cerebellar nuclei at 3 T. (A–D) T_1 -weighted image, T_2 -weighted image, susceptibility-weighted image and susceptibility map. The white box in (A) indicates the region of the enlarged sections in (B–D). The white and black arrows indicate the dentate nucleus and the emboliform nucleus, respectively. [The figure was modified from ref. (166) with permission from Springer.]

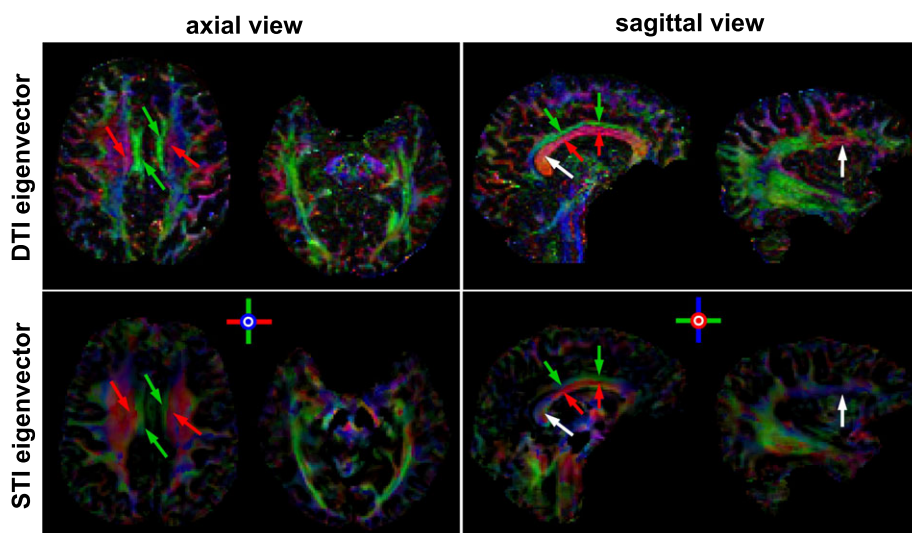


Figure 6. Comparison of the main eigenvectors of diffusion and susceptibility tensors in the human brain. The top row shows fractional anisotropy (FA)-weighted diffusion tensor imaging (DTI) color maps. The bottom row presents susceptibility tensor imaging (STI) eigenvector maps weighted by the rescaled mean susceptibility. The corpus callosum/superior corona radiata and the cingulate gyrus (in axial view), as well as the corpus callosum and the cingulate gyrus (in sagittal view), are clearly separated with consistent orientations between STI and DTI (red and green arrows). Differences also exist (white arrows) which may be caused by imperfect image registration in the STI processing (see bottom row in Fig. 1). [The figure was modified from ref. (35) with permission from Elsevier.]

the depiction of microhemorrhages below the imaging voxel scale, but, on the other, impede accurate lesion size quantification. As QSM overcomes blooming effects, it provides more accurate measurements of the geometrical size of TBI-related lesions and their magnetic susceptibility, although at the cost of detection sensitivity that might be slightly inferior to SWI. In a longitudinal study, Liu *et al.* (175) reported decreased magnetic susceptibility in hemorrhages, indicating continued subtle evolution in the chronic state of TBI. Apart from hemorrhages, the occurrence of selective axonal calcifications has also been reported (176). Furthermore, some subdural hematomas may resorb spontaneously or become calcified 3 weeks or more after

trauma (177). Therefore, the verification of calcifications can identify non-recent hemorrhages. Figure 7 demonstrates the high sensitivity of QSM, even to minute calcifications, which are not expected to be present in recent hemorrhage, thereby allowing improved age dating of trauma in cases of, for example, non-attended injury, including abusive head trauma.

Brain tumors

The ability to identify calcified and hemorrhagic tumor areas, as well as to precisely localize a tumor, may be valuable for the classification and grading of brain tumors (178). From

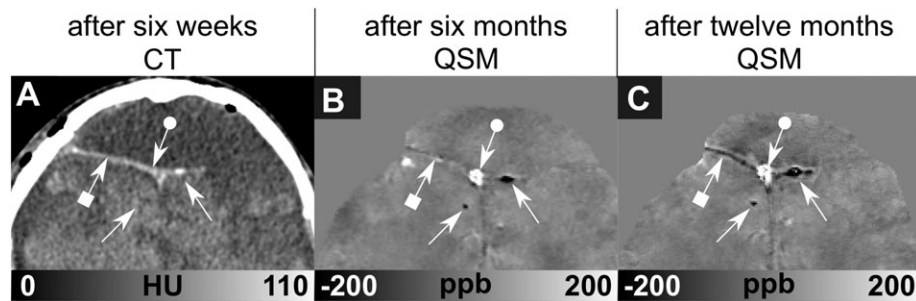


Figure 7. Case of a 2.5-year-old boy who survived a severe traumatic brain injury after falling from a height of 6 m. (A) Computed tomography (CT) scan 6 weeks after the injury. Susceptibility maps of the same slice after 6 months (B) and after 12 months (C). CT (A) confirmed post-traumatic formation of the bifrontal hygroma and discrete calcification [107 Hounsfield units (HU); right-hand-side straight-ended arrow]. Quantitative susceptibility mapping (QSM) delineates several smaller collections of blood (circle-ended arrow) as well as punctate calcifications of the dura mater and adjacent to it (straight-ended arrows). Although the dura mater (square-ended arrow) appeared both isointense and slightly hyperintense on the susceptibility map during the initial MRI (B), it appeared with low intensity on the susceptibility map acquired 12 months after the injury (C), suggesting incomplete blood removal and calcification.

histopathological evaluation as well as CT, oligodendrogliomas, for instance, are known to present intratumoral calcifications (179). As demonstrated in Fig. 8, calcifications in

oligodendrogliomas are also discernible as hypointense intratumoral areas on susceptibility maps. In the study of primary brain neoplasms, especially malignant glioma, the imaging of variations in magnetic susceptibility revealed advantages in depicting the internal architecture encompassing the venous vasculature, blood products, calcification and edema (180). In a more recent study, it was demonstrated with QSM that calcifications also occur in recurrent glioblastoma (153). Of interest within this context is that calcifications have been reported to be common in patients with glioblastoma who are exposed to bevacizumab, a vascular endothelial growth factor neutralizing antibody, and that these lesions may represent a novel biomarker associated with response and improved outcome (181). Consequently, QSM can be used to assess these lesions and to monitor their progression during therapy.

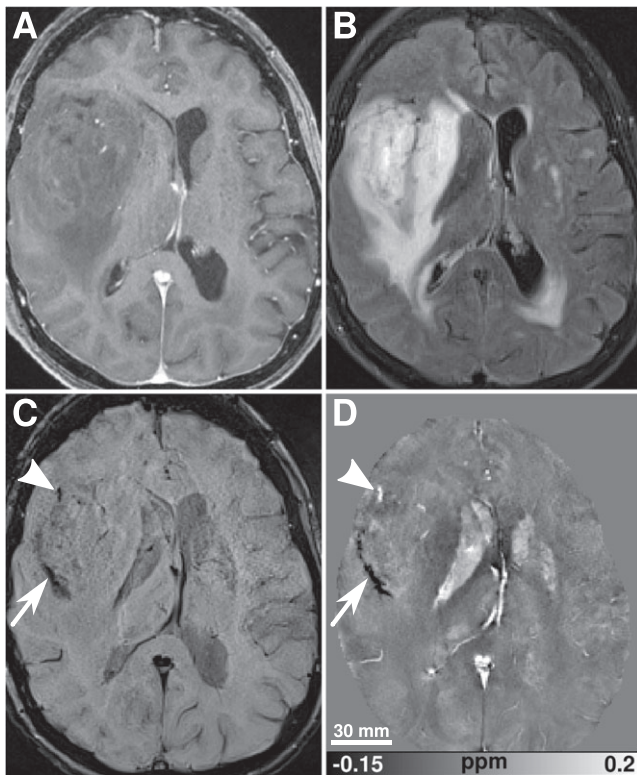


Figure 8. Seventy-four-year-old patient with a right temporal oligodendroglioma. (A) Contrast-enhanced T_1 -weighted image. (B) T_2 -weighted fluid-attenuated inversion recovery (FLAIR) image. (C) Susceptibility-weighted image. (D) Quantitative susceptibility map. Substantial intratumoral susceptibility variations (arrowhead, arrow) are clearly seen with susceptibility-weighted imaging (SWI) and quantitative susceptibility mapping (QSM). Interestingly, these variations show no correlates on the conventional T_1 -weighted and T_2 -weighted FLAIR images. QSM clearly suggests that these susceptibility variations are likely produced by calcium deposits (arrow) and blood products (arrowhead). The MRI data were kindly provided by Alexander Radbruch (Department of Neuroradiology, University of Heidelberg Medical Center, Heidelberg, Germany).

Neurodegenerative diseases

Parkinson's disease

Iron elevation in specific brain regions and selective loss of dopaminergic neurons are major pathological features of Parkinson's disease (PD) (152,182,183). Clinically, transcranial sonography provides a quick, non-invasive and easily applicable, but strongly user-dependent, way to display specific structural changes in selected brain regions (184). Although hyperechogenicity in the anatomical region of the substantia nigra (SN), putatively as a result of increased iron content, is believed to be a biomarker of PD, the biophysical underpinnings are not entirely known (185,186). In comparison with transcranial sonography, quantitative MRI provides a more thorough and standardized characterization of pathological tissue changes. For instance, in line with histological findings (187), QSM indicated increased iron concentrations in the SN of patients with PD, particularly in the pars compacta, with higher sensitivity compared with R_2 or R_2^* maps (152,154,188,189). Thus, QSM might become the MRI method of choice for the identification of the nigrostriatal signature of PD. This may, in particular, hold true with respect to the detection of the nigrosome, which has recently gained interest as it represents a promising substructure of the SN that appears to undergo specific changes, and promises to provide a major change in the clinical practice of how to diagnose PD (190).

Alzheimer's disease

Alzheimer's disease (AD) is associated with elevated cerebral iron content (191–193), where iron occurs, amongst others, as a component of neuritic plaques (194) and neurofibrillary tangles (192). An elevated iron milieu might constitute ideal proliferation and perpetuation environments for β -amyloid aggregation and neurotoxicity (195–197). The ability to estimate iron level variations *in vivo* is thus expected to shed additional light on the onset and development of the disease. However, human studies applying QSM in patients with AD are still scarce. Acosta-Cabronero *et al.* (197) reported significantly increased magnetic susceptibility in deep GM nuclei (particularly putamen) and in posterior GM and WM regions in patients compared with matched controls. Similar findings in the putamen and caudate nucleus were observed by Moon *et al.* (198). One further study reported increased susceptibility values bilaterally in the superior frontal and parietal cortex, right temporal cortex and left precuneus in β -amyloid positron emission tomography (PET)-positive AD patients compared with β -amyloid PET-negative controls (199). Increased cortical susceptibility is supported by a histopathological study that detected increased iron at the earliest detectable signs of cognitive decline in patients with AD, which was localized to amyloid plaques, a small number of neurofibrillary tangles and other intracellular locations (193). Iron-positive amyloid plaques were also found in the cortex of APP/PS1 mice with a wide distribution and could additionally be made visible using T_2^* -weighted MRI (200). As high-resolution T_2^* -weighted MR microscopy at 7 T has indicated

its ability to visualize cortical pathology in patients with AD *in vivo* as well (201), it appears that QSM is well suited to contribute to an improved characterization of the disease in the future.

Multiple sclerosis

Multiple sclerosis (MS), an autoimmune, demyelinating disease of the central nervous system, is known to be associated with increased iron deposition in deep GM nuclei and the occurrence of lesions in both WM and cortical GM (192,202,203). Initial results in patients revealed that QSM is more sensitive to disease-induced tissue changes (e.g. neurodegeneration with brain iron accumulation) than are other quantitative MRI methods, and allows the assessment of tissue changes even at a very early stage of MS (204–207). In line with histological findings (192), increased iron content in deep GM, indicated by QSM, has been reported in patients compared with healthy controls (204–206).

Motivated by the different presentation of lesions on GRE phase images (65,208,209), several recent studies have investigated their appearance on susceptibility maps. Heterogeneous contrast patterns of WM MS lesions (Fig. 9), i.e. the appearance of some lesions with hyperintense signatures, but others with isointense signals, to the surrounding tissue, have been reported (210–212). Furthermore, the appearance of lesions on QSM has been found to be related to lesion age. Chen *et al.* (212) reported that active, enhancing lesions are isointense on susceptibility maps (white arrow in Fig. 9), whereas the very same lesions appear hyperintense after a period of 3 months. The biophysical

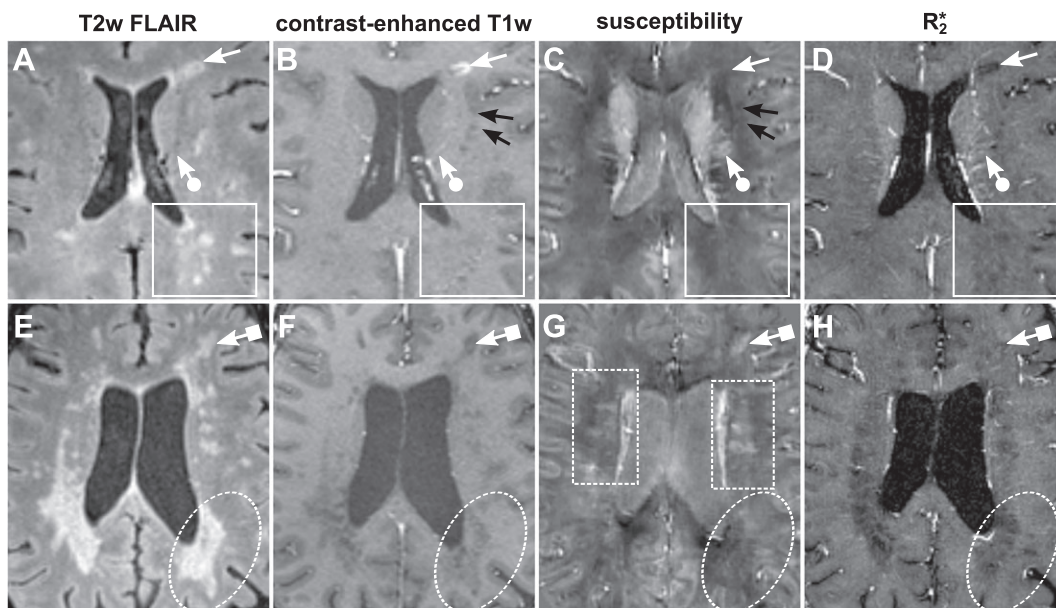


Figure 9. Multimodal imaging of multiple sclerosis (MS) lesions illustrating their different presentation among different MRI contrasts. Top row: MRI of a 42-year-old male patient. Bottom row: MRI of a 33-year-old female patient. (A, E) T_2 -weighted (T2w) fluid-attenuated inversion recovery (FLAIR) images. (B, F) Contrast-enhanced T_1 -weighted (T1w) images. (C, G) Susceptibility maps. (D, H) R_2^* maps. Scaling of the susceptibility maps (C, G) ranges from -100 to 150 ppb, and between 0 and 50 s^{-1} for the R_2^* maps (D, H). Top row: the white arrow points to a contrast-enhancing active lesion on the T1w image. Although this lesion also contrasts on the T2w FLAIR image and R_2^* map, it is not seen on the susceptibility map. The circle-headed white arrow points to a hyperintense lesion on QSM which is barely visible or absent on the other contrasts. In addition, the susceptibility contrast of other MS lesions (white rectangle) is not as striking as on the T2w FLAIR image. Bottom row: the square-headed arrow indicates a lesion that is visible in the T2w FLAIR image, contrast-enhanced T1w image and susceptibility map with a more or less homogeneous pattern. The same lesion, however, is barely seen on the R_2^* map. Venous association of MS lesions can be identified on QSM (dashed-lined rectangles), which is barely or not possible with the other contrasts. R_2^* and QSM may also be consulted to assess the tissue composition of the large lesions seen in T2w FLAIR (e.g. dashed-lined ellipse). However, the predictive value of susceptibility- and R_2^* -based lesion characterization has not yet been proven.

origin of the lesion contrast is, however, difficult to resolve with QSM alone. Iron concentration, myelin content and the microstructure of the lesions all change during the course of the disease (209,213,214), thus affecting the measured phase values and extracted susceptibility. It has, for instance, been demonstrated in a post-mortem study that lesions may appear hyperintense on susceptibility maps if iron is abundant, but that they also do so if only myelin is degraded and iron does not deviate from the surrounding tissue (211). Consequently, QSM in combination with further quantitative MRI contrasts (e.g. relaxation rate maps, magnetization transfer images) is expected to be an important method for disentangling the main contributors of the resulting tissue contrast and its time course, potentially improving the understanding and assessment of pathological alterations during disease progression.

Degenerative cerebellar ataxia

Degenerative cerebellar ataxias are slowly progressive disorders that affect the cerebellum and cerebellar pathways to various degrees (215). Post-mortem histological studies have indicated that the size of the cerebellar nuclei is reduced in Friedreich's ataxia (FRDA), spinocerebellar ataxia (SCA) type 1 (SCA1), SCA3 and SCA6 (216–219). As the shape of the cerebellar nuclei and the internal distribution of iron are likely tightly coupled (220), non-invasive visualization and quantification of these iron distributions offers an elegant possibility to assess the size and volume of the nuclei (166). SWI has recently been applied in healthy subjects to visualize the cerebellar nuclei *in vivo* and to assess their volume (221,222). It also allowed the observation of atrophy of the cerebellar nuclei in patients with FRDA, SCA3 and SCA6 (223). On the other hand, care must be exercised when assessing nuclei volumes based on susceptibility-weighted images because they do not reflect the actual volumes. However, as QSM allows for much improved anatomical delineation of deep GM structures and cerebellar nuclei (see Fig. 5), as well as accurate quantification of iron content (19,21), it will probably further improve the characterization of the cerebellar nuclei in both healthy and diseased subjects, and help to resolve controversial findings of iron changes in degenerative ataxia disease pathology (224–227).

Neurosurgical planning

QSM has already proven its remarkable potential to visualize non-invasively brain areas with excellent distinction, including the substantia nigra pars reticulata, ventral intermediate thalamic nucleus, subthalamic nucleus and the substructures of the internal globus pallidus (64,155,158,228), which represent common targets for deep brain stimulation (DBS). DBS is a stereotactic neurosurgical application, in which electrodes are precisely placed into certain brain structures to alleviate motor disorders caused by tremor, PD or dystonia (229). Typically, these target nuclei are identified using atlases in combination with MRI scans. However, significant differences have been reported between target coordinates extracted using direct targeting MR procedures and those extracted using indirect atlas-based measures (230). Although QSM has not been verified for preoperative planning in DBS to date, it is nevertheless considered as an exciting way to produce high-quality images that aid neurosurgeons to accurately and reliably target the electrodes (161).

QSM outside the brain

As stated previously, to date, most applications of QSM relate to brain imaging. Nevertheless, the characterization of magnetic susceptibility in other body parts is currently an active field of research. Direct transfer of the techniques from the brain to other body parts, however, is hampered by several issues, including cardiac motion, respiratory motion, the presence of fat and/or rapid signal decay (e.g. from severe field distortions).

Sharma *et al.* (113) suggested that magnetic susceptibility may serve as a more direct and robust imaging biomarker of hepatic iron overload, and applied a chemical shift-encoded reconstruction to estimate the field map and incorporated prior information of the fat distribution into the susceptibility mapping algorithm to determine bulk susceptibility in the liver. A linear relationship between MRI-based susceptibility values and both R_2^* values and liver iron concentration estimates obtained from the Food and Drug Administration-approved Ferriscan approach was observed. Although SQUID (superconducting quantum interference device) is a well-validated alternative for the measurement of liver iron concentrations and also measures susceptibilities (231), its use is limited because of the high costs and very restricted availability, with only a few devices currently available worldwide (113). Transverse relaxation rates (e.g. R_2 , R_2^*), however, have demonstrated good correlation with liver iron content, but represent an indirect measure for which different research groups have even obtained different calibration curves because of confounding factors (e.g. spatial resolution) (232–235). The quantification of susceptibility with QSM thus bears the advantage that a fundamental property of materials is extracted, in contrast with empirical relaxation parameters, enabling a more direct measurement of iron concentrations.

Straub *et al.* (236) were able to depict calcifications in prostate cancer using QSM, and reported susceptibility values for prostatic calcifications ranging from -0.16 to -0.82 ppm, which were found to be in good agreement with susceptibility values for calcification. With QSM's ability to differentiate between calcifications and bleeds, it may aid in the differential diagnosis between prostate cancer and benign prostatic hyperplasia (237).

Furthermore, preliminary attempts have also been undertaken to investigate the potential of QSM for the *in vivo* characterization of breast tissue (31,238), kidney (239) and cartilage (240).

METHODOLOGICAL APPLICATIONS OF MAGNETIC SUSCEPTIBILITY MAPS

Currently, there are a number of methodological applications under development that focus on the magnetic susceptibility contrast *in vivo*. Amongst others, these applications include efforts to disentangle the contributions of the different biophysical origins to magnetic susceptibility, mapping of contrast agent concentration, determination of blood oxygenation and improvement of the segmentation of brain tissue structures. The following sections provide a brief overview of some of these approaches.

Mapping of biophysical sources of contrast

The astounding anatomical contrast in susceptibility maps of the human brain predominantly arises from contributions of tissue iron (paramagnetic) and myelin (diamagnetic). The simultaneous presence and even co-localization of these two contributors can,

however, complicate the interpretation of susceptibility changes, as they may occur, for instance, in neurodegenerative diseases, where inflammatory myelin loss and focal iron accumulation may go hand in hand. Consequently, interest exists to disentangle the major biophysical constituents of the MR image contrast with the goal to create highly sensitive markers for iron and myelin, respectively.

When investigating the visual cortex on R_2^* and frequency maps at ultra-high fields, Fukunaga *et al.* (165) noticed the potential to quantify iron in both WM and GM based on these two contrasts. Soon after, Schweser *et al.* (241) proposed a strategy to separate voxel-wise storage iron concentration and myelin concentration from susceptibility and R_2^* maps. Subsequent refinements included an approach to create two novel contrasts, one independent of orientation effects and the other independent of tissue iron concentration, by setting up a three-compartment tissue model with punctate susceptibility inclusions (representing iron) and myelinated axons in a homogenous tissue matrix (242), which enabled the disentangling of the magnetic properties related to iron and myelin architecture based on susceptibility and R_2^* maps. Alternatively, it has also been suggested to incorporate the local myelin concentration based on additionally acquired magnetization transfer images to correct the susceptibility-based iron quantification *in vivo* (64). All of these approaches, however, neglect the potential influence from chemical exchange effects, and therefore still require further validation from post-mortem measurements or other independent measurements of the iron and myelin content.

More recently, Stuber *et al.* (243) demonstrated elegantly in a post-mortem specimen of the cerebral cortex that concomitant analysis of the longitudinal relaxation rate (R_1), R_2^* and magnetic susceptibility has the potential to separate iron and myelin contributions based on a linear model for iron and myelin concentration. The authors used proton-induced X-ray emission (PIXE) to spatially map iron, phosphorus and sulfur elemental concentrations, where the latter two element maps served as estimates for the myelin content. After calibrating the quantitative MRI measures (R_1 , R_2^* , χ) with the PIXE-based iron and myelin maps, the authors succeeded in performing the inverse process of calculating iron and myelin maps from the MR maps with comparably good results. Further research is certainly needed to transfer these promising results to the *in vivo* situation, as well as to verify some of the assumptions made with respect to the quantification of myelin using the PIXE technique.

Contrast agent mapping

The absolute determination of contrast agent concentrations *in vivo* is not trivial, and may be quite important in the field of contrast agent-based, perfusion-weighted imaging and for the characterization of the deposition of functionalized contrast agents in molecular MRI. Contrast agent mapping by exploiting T_1 or T_2 enhancement effects relies on calibration measurements and is highly susceptible to B_1 inhomogeneities (31,244,245). In addition, the theoretical relationship between changes in the transverse relaxation rate and contrast agent concentration is complicated, and depends on many factors, including the size and geometry of the vessels (246). Magnetic susceptibility, however, has the advantage that it should be linearly related to contrast agent concentration and should be independent of vessel orientation (247). Consequently, from a knowledge of the molar

susceptibility of the contrast agent, the concentration of the contrast agent can be derived from the measured induced susceptibility shift. This specific property renders QSM an effective tool for the quantification of contrast agent concentration with MRI. Initial studies have applied this approach to quantify contrast agent concentration changes in bolus-based, time-dependent perfusion imaging, from which cerebral blood flow and cerebral blood volume maps were calculated with reasonable agreement to the maps obtained with conventional analysis of R_2^* and its changes (247,248). Further work, however, is still required to transfer QSM-based perfusion imaging into a clinically relevant tool, as the CNR associated with susceptibility changes is currently limited compared with the established MR perfusion imaging approaches.

The value of QSM in the quantification of iron oxide nanoparticles in biological tissue has recently been proven in several preclinical MRI studies (249,250), where it may be able to uniquely aid the visualization of cellular and molecular processes *in vivo* (251).

Blood oxygenation assessment and functional QSM (fQSM)

Magnetic susceptibility values of venous blood can be directly converted into blood oxygenation saturation (see Equation [24]), an important physiological parameter describing the amount of oxygen dissolved in blood with implications for understanding cerebral physiology and pathophysiology, such as stroke (252) and tumors (253). This has been nicely demonstrated with larger venous vessels, such as, for example, the superior sagittal sinus, with diameters of 5 mm or even larger (254), for which a blood oxygenation of 0.64 ± 0.03 has been derived from susceptibility maps in healthy subjects under resting state conditions (255). This value has recently been confirmed with phase-based susceptometry and alternative T_2 -based oximetry approaches (256,257). Furthermore, it has been shown that blood oxygenation decreases along the venous vessel system, the further the vessel is away from its capillary bed (Fig. 10B) (255,258). However, care should be exercised when estimating oxygenation levels, as QSM may overestimate the magnetic susceptibility up to 10%, in particular for veins oriented close to 45° to the main magnetic field. In addition, blood oxygen changes induced by caffeine ingestion (259), by changing breathing conditions (260) or by performing task-related experiments (261–264) have been quantified with QSM. Such blood oxygenation modulations determined with QSM can be combined with perfusion imaging (e.g. based on arterial spin labeling) to determine oxygen extraction fractions and the cerebral metabolic oxygenation rate (CMRO₂) across selected tissue regions (260), or even whole brain tissue (265), to study local oxygen consumption *in vivo*.

Task-related magnetic susceptibility variations have been investigated for a more direct quantification of brain activation. Chen *et al.* (264) proposed susceptibility-based functional brain mapping by determining a phase activation map followed by field-to-susceptibility inversion. This methodology may be problematic for vessels parallel or at the magic angle with respect to the main magnetic field because, for parallel vessels, the extravascular phase contributions vanish and, for vessels at the magic angle, the intravascular phase is zero (266). The approach of Chen *et al.* (264) may be a reasonable solution as long as phase variations are small ($|\phi| \ll \pi$), which is usually the case for MRI acquisitions at short TEs, low field strength and low spatial

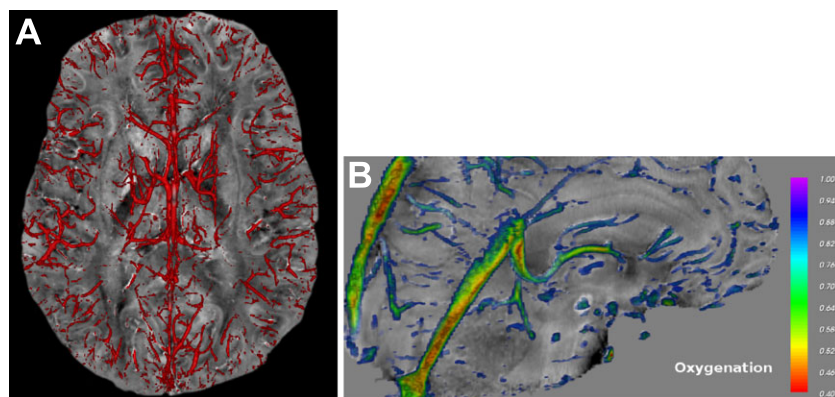


Figure 10. (A) Three-dimensional reconstruction of the vessel network from susceptibility maps showing the cortical and central veins at the level of the thalamus and superior to it. (B) Volume-rendered distribution of blood oxygenation in cerebral veins. The large sinuses show low oxygenation rates of about 50%. Interestingly, the blood oxygenation gradually increases along the vessel path with larger distance from the sinuses to reach more than 80% in the small vessels. [Image (B) is reprinted with permission from ref. (259)].

resolution. Otherwise, the magnetic susceptibility distribution for each three-dimensional volume of the fMRI time course can be reconstructed, and the resulting susceptibility time course statistically analyzed (261,262). This fQSM strategy requires, however, optimized preprocessing to remove unwanted phase signal fluctuations (e.g. caused by physiological noise) prior to the computation of time-resolved susceptibility maps. fQSM enabled the detection of activated voxels in cortical regions and the draining pial and intracortical veins at 7 T (261,262). It was also found that the activation patterns were substantially smaller than those observed with conventional magnitude-based fMRI analysis of the same scan, suggesting a more confined functional localization with the susceptibility-based approach. As the information provided by both fQSM and conventional fMRI can be extracted from the same complex-valued time series, concomitant analysis is expected to provide further insight into the structure–function relationship *in vivo*. However, as fMRI usually relies on two-dimensional EPI acquisitions, the application of three-dimensional post-processing methods (such as phase unwrapping or background field removal) typically associated with QSM reconstruction may result in slice to slice inconsistencies that potentially affect task-related susceptibility changes (267). Therefore, further investigations of fQSM, in particular with respect to data analysis and sensitivity at lower magnetic fields, are certainly needed to explore the full potential of the technique.

Mapping structures with short relaxation times

Susceptibility mapping of tissues with short relaxation times ($T_2^* < 5$ ms), such as bone or teeth, is practically not feasible with conventionally used echo times in GRE imaging and established susceptibility computation approaches (see ‘Computational strategies for determination of magnetic susceptibility’ section) because of the low MR signals with limited SNR, and hence unreliable phase values. As one strategy to overcome this limitation, Buch *et al.* (268) combined high-bandwidth, short-TE GRE imaging with an iterative computational approach that links the inverse problem (field-to-susceptibility computation) with the forward problem (susceptibility-to-field computation). Field values of regions with high SNR (e.g. brain tissue) and predicted field values of low-SNR regions (e.g. skull, sinuses) for which the susceptibilities are sought are simultaneously used to reconstruct the local susceptibility. Field values in the low-SNR regions of

interest are iteratively updated using fast-forward field calculation, and computation of susceptibility is repeated until convergence is reached. With this approach, the authors determined the average magnetic susceptibility differences of air in the sinuses ($\Delta\chi = 7$ – 9.5 ppm), skull bone ($\Delta\chi = -2.1$ ppm) and teeth ($\Delta\chi = -3.3$ ppm) with respect to brain tissue. This method could open up a new avenue to determine the magnetic properties of substances without water protons, and may offer a possibility to quantify the magnetic susceptibility of solid objects as long as they reveal susceptibility differences with their surrounding materials.

An alternative way to characterize tissues with short relaxation times is to apply ultrashort-TE GRE sequences (269), which enable the extraction of reliable phase values from which the magnetic susceptibility can be reconstructed. This has recently been demonstrated with bovine cortical bone samples embedded in agarose gel (270).

Image processing applications

The exquisite contrast and detail of anatomical structures seen on susceptibility maps suggest application in image processing to improve the reliability of the automatic identification of anatomic (sub)structures for parameterization and three-dimensional visualization of GM parameters. Recently, a combination of magnetic susceptibility maps and T_1 -weighted images has been proposed to create a composite image to feed FMRIB’s integrated registration and segmentation tool (FIRST) (271) with the aim to improve the segmentation accuracy of deep GM regions (272). As seen from Fig. 11, the incorporation of the susceptibility information resulted in a more precise segmentation of subcortical structures.

Extraction of the venous vessel network from QSM is also possible (Fig. 10A) and provides a first step to the quantification and parameterization of the venous macro-vasculature (273). The combination of three-dimensional, high-resolution information on individual venous vessels and deep GM structures is expected to support neurosurgical interventions because of the improved visualization of these complex anatomical structures.

LIMITATIONS AND FUTURE DIRECTIONS

One of the main drawbacks of susceptibility mapping is that it provides relative rather than absolute values of magnetic

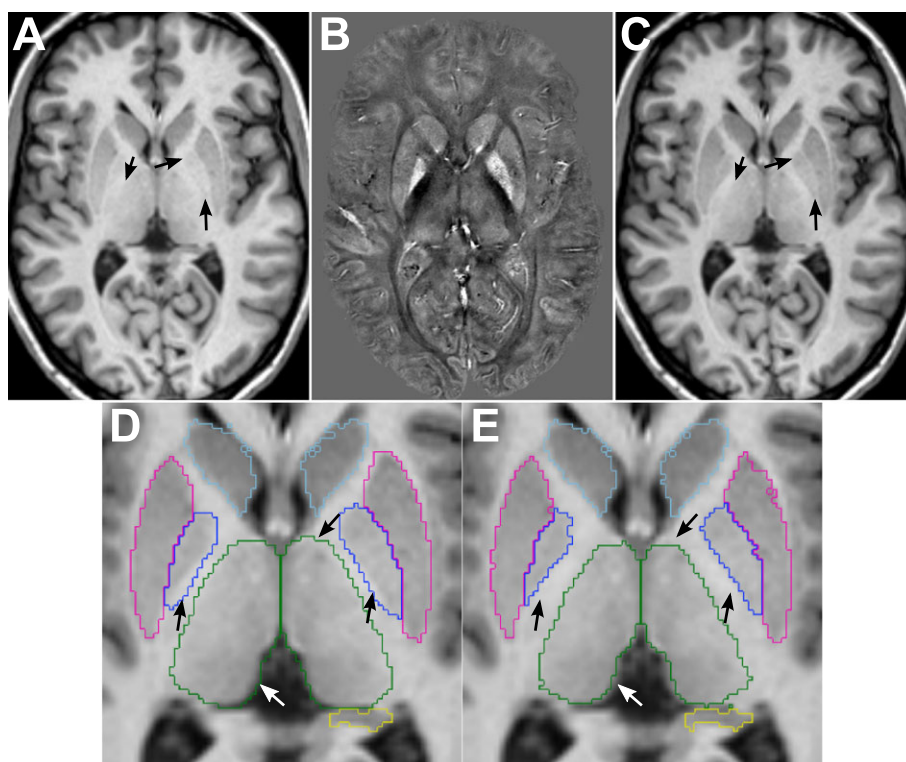


Figure 11. Utilization of magnetic susceptibility contrast to improve subcortical segmentation. Conventional T_1 -weighted image (A), susceptibility map (B) and composite image generated by linearly combining T_1 -weighted (A) and susceptibility (B) information (C). Black arrows in (A) and (C) indicate improved delineation of the globus pallidus and thalamus with respect to the surrounding white matter in (C). The subcortical segmentation results obtained using FMRIB's integrated registration and segmentation tool (FIRST) based on T_1 -weighted images and the composite images are shown as overlays on the composite images in (D) and (E), respectively. The black and white arrows in (D) and (E) indicate the increased segmentation accuracy for the globus pallidus and thalamus in (E).

susceptibility. As the maps have an unknown offset, owing to the fact that the k -space origin of the computed susceptibility map is undefined, susceptibilities must be referenced to a particular region or tissue, which may hamper inter-subject comparisons. The appropriate choice of the reference region is still an unsolved problem. Selecting cerebrospinal fluid (CSF) in the ventricles as a reference region may seem an elegant choice at first sight. The ventricles, however, are traversed by the choroid plexuses, which contain iron in their stroma (274), which may lead to heterogeneous patterns on susceptibility maps. As a consequence, when probing different brain regions (e.g. CSF, putamen, large veins, global WM, frontal deep WM, occipital WM) to serve as reference regions across a multitude of VOIs of similarly aged subjects, the least inter-subject variation was not observed for CSF, but for frontal WM (158). On the other hand, as neurological or psychiatric diseases affect brain tissue, including WM and its anisotropy, this issue must be considered when choosing the reference region. The problem of referencing has certainly to be further explored in future studies.

Accurate and careful data preprocessing is important before application of the field-to-susceptibility inversion. The demarcation of regions with internal magnetic field variations, which is essential for background field removal (see 'Background field removal' section), and the identification of unreliable phase values are both important details that require special consideration. The first issue may be solved using existing skull stripping tools, such as the FMRIB Software Library's brain extraction tool (275), BEaST (276) or Freesurfer (277), to identify brain tissue, followed by dedicated post-processing to resolve potentially

incorrectly segmented voxels. In other body regions, such as the abdomen, the definition of the internal field region is usually based on thresholding, which is often user dependent. The second issue may be solved by evaluating the temporal phase evolution and SNR in the magnitude images (64).

A variety of field-to-susceptibility inversion approaches exist (see 'From tissue magnetic field perturbation to bulk magnetic susceptibility' section), all having their own advantages and disadvantages. One major demand on any inversion algorithm is its ability to reconstruct subtle tissue susceptibility variations whilst simultaneously suppressing artifacts, such as streaking and potential blooming, to avoid that these non-local artifacts are mistaken as pathological abnormalities. However, depending on the type of algorithm, the effective spatial resolution of the susceptibility maps might be inferior to that of the original magnitude and background-corrected phase images. Severe or improper regularization typically results in rather smooth susceptibility maps (106). As a consequence, the CNR and the demarcation of small structures with subtle susceptibility variations are diminished. Therefore, further development of effective regularization approaches with appropriate adjustment is still required.

As already alluded to above, anisotropic susceptibility and microstructural anisotropy can contribute substantially to the contrast in frequency maps (128). If such frequency (or phase) maps are used as input to currently applied QSM or STI reconstruction algorithms, artificial heterogeneities in the susceptibility maps or substantial overestimation of the estimated susceptibility anisotropy may result because of the implicitly

assumed isotropy in the former and the neglect of the microstructure in the latter. In the mentioned study, it was nicely demonstrated that the standard deviations of susceptibility values in WM, determined from the difference images between susceptibility maps calculated from different frequency maps and the reference distribution of isotropic susceptibilities, increased substantially when successively considering isotropic, isotropic and anisotropic susceptibility and finally adding the microstructural contribution. These observations require further investigations with regard to the development of novel approaches of tissue modeling and reconstruction that are able to handle these issues. Unfortunately, there seems to be no unique or generally accepted and manageable solution currently available.

One further issue, often neglected in QSM, concerns subject movement and physiological motion during the rather long acquisition of three-dimensional GRE data, which have been shown to introduce phase shifts that cannot be explained with the field-to-susceptibility model, and ultimately lead to inaccurate susceptibility maps. To account for movements, prospective methods for real-time motion correction based on external optical motion tracking systems (278,279) and retrospective motion correction approaches (280,281) have already been introduced. Physiological fluctuations, such as changes in the blood flow and blood oxygenation level, as well as respiration-induced organ motion, give rise to local magnetic field variations which have been perceived as important factors of MR image quality (282,283). The incorporation of navigator measurements (282,283) or concurrent field monitoring with NMR probes (284,285) during the acquisition has been demonstrated to successfully reduce artifacts in GRE imaging.

Although initial work has already been undertaken to assess the accuracy of field-to-susceptibility inversion strategies (31) and to demonstrate the reproducibility of QSM (286–288), systematic evaluation and critical comparison of the accuracy, inter-subject variability and intra-subject reproducibility still remain an issue (28). The in-depth characterization of algorithm performance and its dependence on MR pulse sequences may finally converge to an acceptable standard for susceptibility mapping, facilitating integration into clinical routine. This endeavor, however, certainly requires concerted efforts across multiple imaging centers and different vendors.

Although STI and its extension GLTA are limited for applications *in vivo* because of the need for multiple orientation measurements, they are promising for the characterization of tissue microstructure in animals and post-mortem tissue samples. STI and GLTA will most probably improve our understanding of magnetic susceptibility contrast and assessment of inaccuracies obtained with single-angle QSM by figuring out the tissue types for which a consideration of susceptibility anisotropy and/or microstructural anisotropy is necessary. In an interesting attempt to overcome the need to acquire multiple orientation scans for the assessment of anisotropy, Liu and Li (289) suggested the imposition of field gradients by shifting the *k*-space of a single dataset to uncover tissue microstructural information of magnetic susceptibility (*p*-space imaging). Numerical simulations have, however, subsequently demonstrated that *p*-space imaging does not appear to be directly linked to the susceptibility of the axon compartment, but may be applied to detect voxel substructures and strong dephasing effects from bulk isotropic susceptibility sources (290,291).

From a clinical point of view, unambiguous assignment of the biophysical sources responsible for the pattern seen on susceptibility maps is of particular interest. One main strength of QSM is the ability to differentiate between blood deposits and calcifications, which promises to facilitate (differential) diagnosis and monitoring of therapy. Variations of myelin and iron, however, cannot be unequivocally disentangled solely with QSM because of the complexity of brain tissue. Although myelin mainly determines the susceptibility contrast in WM, iron is also present in oligodendrocytes. Likewise, there is a significant amount of myelinated fibers present in deep GM, but their magnetic susceptibility contribution is superposed by the more paramagnetic susceptibility of iron. MS lesions represent a clinical example in which the assessment of the biophysical contrast sources, i.e. iron increase, demyelination or tissue microstructure loss, is of particular interest. Concomitant analysis of multiple quantitative image contrasts, such as R_1 , magnetization transfer ratio, R_2^* and/or susceptibility maps, is expected to be a valuable asset in solving these problems.

As myelination and iron depositions change during the life span, a knowledge of these trajectories of magnetic susceptibility is beneficial to establish QSM as a quantitative tool in the clinic. Individual areas on susceptibility maps could be compared with normative values or age-specific susceptibility templates generated from a healthy population to facilitate the identification of abnormal magnetic susceptibility. This process could be automated and exploited in computer-aided diagnosis to support the clinicians in decision making.

So far, susceptibility investigations have mainly focused on the human brain. However, it is anticipated that mapping of magnetic susceptibility or its anisotropy may also reveal valuable information in other parts of the human body (e.g. liver, kidney, breast and spine). To make susceptibility investigations more applicable in future development, there is a need to establish dedicated fast imaging techniques (e.g. GRE with EPI, GRE with wave-CAIPI) to improve speed, spatial resolution and coverage, in combination with sophisticated reconstruction techniques to account, for example, for the chemical shift effects from fat.

CONCLUSIONS

The emerging techniques QSM and STI enable the characterization of tissue magnetic susceptibility *in vivo*. Both techniques are currently not yet commercially available on MRI systems from vendors, but dedicated software packages have been released by several working groups (292–295). Although STI will most probably find application in scientific neuroimaging and preclinical imaging, QSM is expected to play an increasing role in the clinic, similar to SWI. QSM has the potential to provide unique etiological and diagnostic information on tissue compositional changes in neurodegenerative diseases as well as in the ageing brain, to unambiguously differentiate between calcified and hemorrhagic lesions, to aid in differential diagnosis and to reveal brain anatomy useful for refining current stereotactic targeting or image segmentation approaches. Apart from this enormous clinical potential, quantitative imaging of magnetic susceptibility may also be exploited to improve existing MRI techniques to enable highly localized imaging of cerebral activation in fMRI experiments (i.e. fQSM), contrast agent concentration mapping for tumor assessment or in molecular MRI, and quantitative perfusion imaging. With the advent of faster imaging techniques

and more sophisticated post-processing techniques, the application field of QSM will most likely expand from the brain to other organs of the human body.

Acknowledgements

We are deeply grateful for support from Berengar W. Lehr, Li Huang, Karsten Sommer, Xiang Feng, Barthelemy Serres, Martin Stenzel, Hans-Joachim Mentzel, Matthias Schwab, Andreas Schäfer, Robert Turner, Dagmar Timmann, Jan Klohs, Till Schneider and Alexander Radbruch. We acknowledge funding from the German Research Foundation (DFG, RE1123/9-2, DE2516/1-1), seed grants awarded to F.S. by the International Society for Magnetic Resonance in Medicine (ISMRM) and the Friedrich Schiller University Jena, and a seed grant awarded to A.D. by the Interdisciplinary Center for Clinical Research (IZKF) in Jena, Germany. Support is also acknowledged from the bilateral PPP–USA 2015/2016 program (project 57131995–Quantitative MRI for Neurological Studies) of the German Academic Exchange Service (DAAD) awarded to JRR.

REFERENCES

1. Faul D, Abart J, Margosian P. Quick measurement of magnetic field variations within the body. *Radiology* 1984; 153(P): 303.
2. Cox IJ, Bydder GM, Gadian DG, Young IR, Proctor E, Williams SR, Hart I. The effect of magnetic susceptibility variations in NMR imaging and NMR spectroscopy in vivo. *J. Magn. Reson.* (1969) 1986; 70(1): 163–168.
3. Young IR, Bydder GM, Khenia S, Collins AG. Assessment of phase and amplitude effects due to susceptibility variations in MR imaging of the brain. *J. Comput. Assist. Tomogr.* 1989; 13(3): 490–494.
4. Yamada N, Imakita S, Nishimura T, Takamiya M, Naito H. Evaluation of the susceptibility effect on gradient echo phase images in vivo: a sequential study of intracerebral hematoma. *Magn. Reson. Imaging* 1992; 10(4): 559–571.
5. Holt RW, Diaz PJ, Duerk JL, Bellon EM. MR susceptometry: an external-phantom method for measuring bulk susceptibility from field-echo phase reconstruction maps. *J. Magn. Reson. Imaging* 1994; 4(6): 809–818.
6. Sepulveda NG, Thomas IM, Wikswo JP. Magnetic-susceptibility tomography for 3-dimensional imaging of diamagnetic and paramagnetic objects. *IEEE Trans. Magn.* 1994; 30(6): 5062–5069.
7. Hwang SN, Wehrli FW. The calculation of the susceptibility-induced magnetic-field from 3D NMR images with applications to trabecular bone. *J. Magn. Reson. Ser. B* 1995; 109(2): 126–145.
8. Young IR, Khenia S, Thomas DG, Davis CH, Gadian DG, Cox IJ, Ross BD, Bydder GM. Clinical magnetic susceptibility mapping of the brain. *J. Comput. Assist. Tomogr.* 1987; 11(1): 2–6.
9. Jezzard P, Clare S. Sources of distortion in functional MRI data. *Hum. Brain Mapp.* 1999; 8(2–3): 80–85.
10. Reichenbach JR, Venkatesan R, Yablonskiy DA, Thompson MR, Lai S, Haacke EM. Theory and application of static field inhomogeneity effects in gradient-echo imaging. *J. Magn. Reson. Imaging* 1997; 7(2): 266–279.
11. Schenck JF. Physical interactions of static magnetic fields with living tissues. *Prog. Biophys. Mol. Biol.* 2005; 87(2–3): 185–204.
12. Schenck JF. The role of magnetic susceptibility in magnetic resonance imaging: MRI magnetic compatibility of the first and second kinds. *Med. Phys.* 1996; 23(6): 815–850.
13. Haacke EM, Xu Y, Cheng YC, Reichenbach JR. Susceptibility weighted imaging (SWI). *Magn. Reson. Med.* 2004; 52(3): 612–618.
14. Reichenbach JR, Venkatesan R, Schillinger DJ, Kido DK, Haacke EM. Small vessels in the human brain: MR venography with deoxyhemoglobin as an intrinsic contrast agent. *Radiology* 1997; 204(1): 272–277.
15. Ogawa S, Menon RS, Kim SG, Ugurbil K. On the characteristics of functional magnetic resonance imaging of the brain. *Annu. Rev. Biophys. Biomol. Struct.* 1998; 27: 447–474.
16. Yamada N, Imakita S, Sakuma T, Takamiya M. Intracranial calcification on gradient-echo phase image: depiction of diamagnetic susceptibility. *Radiology* 1996; 198(1): 171–178.
17. Deistung A, Mentzel HJ, Rauscher A, Witoszynskij S, Kaiser WA, Reichenbach JR. Demonstration of paramagnetic and diamagnetic cerebral lesions by using susceptibility weighted phase imaging (SWI). *Z. Med. Phys.* 2006; 16(4): 261–267.
18. Schweser F, Deistung A, Lehr BW, Reichenbach JR. Differentiation between diamagnetic and paramagnetic cerebral lesions based on magnetic susceptibility mapping. *Med. Phys.* 2010; 37(10): 5165–5178.
19. Langkammer C, Schweser F, Krebs N, Deistung A, Goessels W, Scheurer E, Sommer K, Reishofer G, Yen K, Fazekas F, Ropele S, Reichenbach JR. Quantitative susceptibility mapping (QSM) as a means to measure brain iron? A post mortem validation study. *Neuroimage* 2012; 62(3): 1593–1599.
20. Schenck JF. Magnetic resonance imaging of brain iron. *J. Neurol. Sci.* 2003; 207(102) (1–2): 99.
21. Zheng W, Nichol H, Liu S, Cheng YC, Haacke EM. Measuring iron in the brain using quantitative susceptibility mapping and X-ray fluorescence imaging. *Neuroimage* 2013; 78: 68–74.
22. Sun H, Walsh AJ, Lebel RM, Blevins G, Catz I, Lu JQ, Johnson ES, Emery DJ, Warren KG, Wilman AH. Validation of quantitative susceptibility mapping with Perl's iron staining for subcortical gray matter. *Neuroimage* 2015; 105: 486–492.
23. Mittal S, Wu Z, Neelavalli J, Haacke EM. Susceptibility-weighted imaging: technical aspects and clinical applications, part 2. *Am. J. Neuroradiol.* 2009; 30(2): 232–252.
24. Duyn JH, van Gelderen P, Li TQ, de Zwart JA, Koretsky AP, Fukunaga M. High-field MRI of brain cortical substructure based on signal phase. *Proc. Natl. Acad. Sci.* 2007; 104(28): 11 796–11 801.USA
25. Robitaille PM, Abduljalil AM, Kangarlou A, Zhang X, Yu Y, Burgess R, Bair S, Noa P, Yang L, Zhu H, Palmer B, Jiang Z, Chakeres DM, Spigos D. Human magnetic resonance imaging at 8 T. *NMR Biomed.* 1998; 11(6): 263–265.
26. Abduljalil AM, Schmalbrock P, Novak V, Chakeres DW. Enhanced gray and white matter contrast of phase susceptibility-weighted images in ultra-high-field magnetic resonance imaging. *J. Magn. Reson. Imaging* 2003; 18(3): 284–290.
27. Deistung A, Rauscher A, Sedlacik J, Stadler J, Witoszynskij S, Reichenbach JR. Susceptibility weighted imaging at ultra high magnetic field strengths: theoretical considerations and experimental results. *Magn. Reson. Med.* 2008; 60(5): 1155–1168.
28. Liu C, Li W, Tong KA, Yeom KW, Kuzminski S. Susceptibility-weighted imaging and quantitative susceptibility mapping in the brain. *J. Magn. Reson. Imaging* 2015; 42(1): 23–41.
29. Schweser F, Deistung A, Reichenbach JR. Foundations of MRI phase imaging and processing for Quantitative Susceptibility Mapping (QSM). *Z. Med. Phys.* 2016; 26(1): 6–34.
30. Duyn J. MR susceptibility imaging. *J. Magn. Reson.* 2013; 229: 198–207.
31. Wang Y, Liu T. Quantitative susceptibility mapping (QSM): decoding MRI data for a tissue magnetic biomarker. *Magn. Reson. Med.* 2015; 73(1): 82–101.
32. Liu C, Wei H, Gong NJ, Cronin M, Dibb R, Decker K. Quantitative susceptibility mapping: contrast mechanisms and clinical applications. *Tomography* 2015; 1(1): 3–17.
33. Haacke EM, Liu S, Buch S, Zheng W, Wu D, Ye Y. Quantitative susceptibility mapping: current status and future directions. *Magn. Reson. Imaging* 2015; 33(1): 1–25.
34. Liu C. Susceptibility tensor imaging. *Magn. Reson. Med.* 2010; 63(6): 1471–1477.
35. Li W, Wu B, Avram AV, Liu C. Magnetic susceptibility anisotropy of human brain in vivo and its molecular underpinnings. *Neuroimage* 2012; 59(3): 2088–2097.
36. Lonsdale K. Diamagnetic anisotropy of organic molecules. *Proc. R. Soc. London, Ser. A* 1939; 171(947): 541–568.
37. Jain M, Gupta R, Gupta A, Kumar M. *Diamagnetic Susceptibility and Anisotropy of Inorganic and Organometallic Compounds*. Springer-Verlag: Berlin, Heidelberg, 2007.
38. Dibb R, Qi Y, Liu C. Magnetic susceptibility anisotropy of myocardium imaged by cardiovascular magnetic resonance reflects the anisotropy of myocardial filament alpha-helix polypeptide bonds. *J. Cardiovasc. Magn. Reson.* 2015; 17: 60.
39. Lorentz HA. *The Theory of Electrons and its Applications to the Phenomena of Light and Radiant Heat*. Teubner BG: Leipzig, 1916.

40. Durrant CJ, Hertzberg MP, Kuchel PW. Magnetic susceptibility: further insights into macroscopic and microscopic fields and the sphere of Lorentz. *Concept Magn. Reson. A* 2003; 18a(1): 72–95.
41. Ulrich R, Glaser RW, Ulrich AS. Susceptibility corrections in solid state NMR experiments with oriented membrane samples. Part II: theory. *J. Magn. Reson.* 2003; 164(1): 115–127.
42. Cook DM. Properties of Matter III: Magnetization. The Theory of the Electromagnetic Field. Prentice-Hall, Inc.: Englewood Cliffs, NJ; 1975, pp. 289–324.
43. Salomir R, De Senneville BD, Moonen CTW. A fast calculation method for magnetic field inhomogeneity due to an arbitrary distribution of bulk susceptibility. *Concept Magn. Reson. B* 2003; 19b(1): 26–34.
44. Li L, Leigh JS. Quantifying arbitrary magnetic susceptibility distributions with MR. *Magn. Reson. Med.* 2004; 51(5): 1077–1082.
45. Marques JP, Bowtell R. Application of a Fourier-based method for rapid calculation of field inhomogeneity due to spatial variation of magnetic susceptibility. *Concept Magn. Reson. B* 2005; 25b(1): 65–78.
46. Shmueli K, Dodd SJ, Li TQ, Duyn JH. The contribution of chemical exchange to MRI frequency shifts in brain tissue. *Magn. Reson. Med.* 2011; 65(1): 35–43.
47. Leutritz T, Hilfert L, Smalla KH, Speck O, Zhong K. Accurate quantification of water–macromolecule exchange induced frequency shift: effects of reference substance. *Magn. Reson. Med.* 2013; 69(1): 263–268.
48. Zhong K, Leupold J, von Elverfeldt D, Speck O. The molecular basis for gray and white matter contrast in phase imaging. *Neuroimage* 2008; 40(4): 1561–1566.
49. Haacke EM, Brown RW, Thompson MR, Venkatesan R. Magnetic properties of tissues: theory and measurements. In *Magnetic Resonance Imaging – Physical Principles and Sequence Design*, 1st edn. John Wiley & Sons, Inc.: New York; 1999, pp. 741–780.
50. Wu B, Li W, Avram AV, Gho SM, Liu C. Fast and tissue-optimized mapping of magnetic susceptibility and T2* with multi-echo and multi-shot spirals. *Neuroimage* 2012; 59(1): 297–305.
51. Liu T, Wisniewski C, Lou M, Chen W, Spincemaille P, Wang Y. Nonlinear formulation of the magnetic field to source relationship for robust quantitative susceptibility mapping. *Magn. Reson. Med.* 2013; 69(2): 467–476.
52. Xu B, Liu T, Spincemaille P, Prince M, Wang Y. Flow compensated quantitative susceptibility mapping for venous oxygenation imaging. *Magn. Reson. Med.* 2014; 72(2): 438–445.
53. Wu D, Liu S, Buch S, Ye Y, Dai Y, Haacke EM. A fully flow-compensated multi-echo susceptibility-weighted imaging sequence: the effects of acceleration and background field on flow compensation. *Magn. Reson. Med.* 2015 [Epub ahead of print]. DOI:10.1002/mrm.25878.
54. Deistung A, Dittich E, Sedlacik J, Rauscher A, Reichenbach JR. ToF-SWI: simultaneous time of flight and fully flow compensated susceptibility weighted imaging. *J. Magn. Reson. Imaging* 2009; 29(6): 1478–1484.
55. Sun H, Wilman AH. Quantitative susceptibility mapping using single-shot echo-planar imaging. *Magn. Reson. Med.* 2015; 73(5): 1932–1938.
56. Langkammer C, Bredies K, Poser BA, Barth M, Reishofer G, Fan AP, Bilgic B, Fazekas F, Mainero C, Ropele S. Fast quantitative susceptibility mapping using 3D EPI and total generalized variation. *Neuroimage* 2015; 111: 622–630.
57. Bilgic B, Gagoski BA, Cauley SF, Fan AP, Polimeni JR, Grant PE, Wald LL, Setsompop K. Wave-CAIPI for highly accelerated 3D imaging. *Magn. Reson. Med.* 2015; 73(6): 2152–2162.
58. Bilgic B, Xie L, Dobb R, Langkammer C, Mutluy A, Ye H, Polimeni JR, Augustinack J, Liu C, Wald LL, Setsompop K. Rapid multi-orientation quantitative susceptibility mapping. *Neuroimage* 2016; 125: 1131–1141.
59. Lim IA, Li X, Jones CK, Farrell JA, Vikram DS, van Zijl PC. Quantitative magnetic susceptibility mapping without phase unwrapping using WASSR. *Neuroimage* 2014; 86: 265–279.
60. Lee J, Fukunaga M, Duyn JH. Improving contrast to noise ratio of resonance frequency contrast images (phase images) using balanced steady-state free precession. *Neuroimage* 2011; 54(4): 2779–2788.
61. Walsh DO, Gmitro AF, Marcellin MW. Adaptive reconstruction of phased array MR imagery. *Magn. Reson. Med.* 2000; 43(5): 682–690.
62. Liu J, Rudko DA, Gati JS, Menon RS, Drangova M. Inter-echo variance as a weighting factor for multi-channel combination in multi-echo acquisition for local frequency shift mapping. *Magn. Reson. Med.* 2015; 73(4): 1654–1661.
63. Koopmans PJ, Manniesing R, Niessen WJ, Viergever MA, Barth M. MR venography of the human brain using susceptibility weighted imaging at very high field strength. *MAGMA* 2008; 21(1–2): 149–158.
64. Schweser F, Deistung A, Lehr BW, Reichenbach JR. Quantitative imaging of intrinsic magnetic tissue properties using MRI signal phase: an approach to in vivo brain iron metabolism? *Neuroimage* 2011; 54(4): 2789–2807.
65. Hammond KE, Lupo JM, Xu D, Metcalf M, Kelley DA, Pelletier D, Chang SM, Mukherjee P, Vigneron DB, Nelson SJ. Development of a robust method for generating 7.0 T multichannel phase images of the brain with application to normal volunteers and patients with neurological diseases. *Neuroimage* 2008; 39(4): 1682–1692.
66. Robinson S, Grabner G, Witoszynskyj S, Trattnig S. Combining phase images from multi-channel RF coils using 3D phase offset maps derived from a dual-echo scan. *Magn. Reson. Med.* 2011; 65(6): 1638–1648.
67. de Zwart JA, van Gelderen P, Kellman P, Duyn JH. Application of sensitivity-encoded echo-planar imaging for blood oxygen level-dependent functional brain imaging. *Magn. Reson. Med.* 2002; 48(6): 1011–1020.
68. Bernstein MA, Grgic M, Brosnan TJ, Pelc NJ. Reconstructions of phase contrast, phased array multicoil data. *Magn. Reson. Med.* 1994; 32(3): 330–334.
69. Thunberg P, Karlsson M, Wigstrom L. Comparison of different methods for combining phase-contrast images obtained with multiple coils. *Magn. Reson. Imaging* 2005; 23(7): 795–799.
70. Moser E, Stahlberg F, Ladd ME, Trattnig S. 7-T MR—from research to clinical applications? *NMR Biomed.* 2012; 25(5): 695–716.
71. Roemer PB, Edelstein WA, Hayes CE, Souza SP, Mueller OM. The NMR phased array. *Magn. Reson. Med.* 1990; 16(2): 192–225.
72. Ros C, Witoszynskyj S, Herrmann K, Reichenbach JR. Reconstruction of phase images for GRAPPA accelerated magnetic resonance imaging. 4th European Conference of the International Federation for Medical and Biological Engineering ECIFMBE 2008, IFMBE Proceedings. Springer-Verlag GmbH: Berlin Heidelberg; 2009, pp. 803–806.
73. Pruessmann KP, Weiger M, Scheidegger MB, Boesiger P. SENSE: sensitivity encoding for fast MRI. *Magn. Reson. Med.* 1999; 42(5): 952–962.
74. Liu S, Ye Y, Buch S, Haacke EM. Multi-channel data combination with linear phase baseline correction. *Proceedings of the 23rd Annual Meeting ISMRM, Toronto, ON, Canada, 2015*; 3309.
75. Ma YJ, Liu WT, Zhao XN, Tang WN, Zhang ZH, Tang X, Fan Y, Li HJ, Gao JH. Improved adaptive reconstruction of multichannel MR images. *Med. Phys.* 2015; 42(2): 637–644.
76. Ghiglia DC, Romero LA. Minimum L(p)-norm two-dimensional phase unwrapping. *J. Opt. Soc. Am. A* 1996; 13(10): 1999–2013.
77. Xiang QS. Temporal phase unwrapping for CINE velocity imaging. *J. Magn. Reson. Imaging* 1995; 5(5): 529–534.
78. Robinson S, Schodl H, Trattnig S. A method for unwrapping highly wrapped multi-echo phase images at very high field: UMPIRE. *Magn. Reson. Med.* 2014; 72(1): 80–92.
79. Abdul-Rahman HS, Gdeisat MA, Burton DR, Lalor MJ, Lilley F, Moore CJ. Fast and robust three-dimensional best path phase unwrapping algorithm. *Appl. Optics* 2007; 46(26): 6623–6635.
80. Witoszynskyj S, Rauscher A, Reichenbach JR, Barth M. Phase unwrapping of MR images using Phi UN—a fast and robust region growing algorithm. *Med. Image Anal.* 2009; 13(2): 257–268.
81. Bioucas-Dias JM, Valadao G. Phase unwrapping via graph cuts. *IEEE Trans. Image Process.* 2007; 16(3): 698–709.
82. Schofield MA, Zhu Y. Fast phase unwrapping algorithm for interferometric applications. *Opt. Lett.* 2003; 28(14): 1194–1196.
83. Navarro MA, Estrada JC, Servin M, Quiroga JA, Vargas J. Fast two-dimensional simultaneous phase unwrapping and low-pass filtering. *Opt. Express* 2012; 20(3): 2556–2561.
84. Cheng Z, Liu D, Yang Y, Ling T, Chen X, Zhang L, Bai J, Shen Y, Miao L, Huang W. Practical phase unwrapping of interferometric fringes based on unscented Kalman filter technique. *Opt. Express* 2015; 23(25): 32 337–32 349.
85. Li L, Leigh JS. High-precision mapping of the magnetic field utilizing the harmonic function mean value property. *J. Magn. Reson.* 2001; 148(2): 442–448.

86. Li W, Avram AV, Wu B, Xiao X, Liu C. Integrated Laplacian-based phase unwrapping and background phase removal for quantitative susceptibility mapping. *NMR Biomed.* 2014; 27(2): 219–227.
87. Wen Y, Zhou D, Liu T, Spincemaille P, Wang Y. An iterative spherical mean value method for background field removal in MRI. *Magn. Reson. Med.* 2014; 72(4): 1065–1071.
88. Liu T, Khalidov I, de Rochefort L, Spincemaille P, Liu J, Tsiouris AJ, Wang Y. A novel background field removal method for MRI using projection onto dipole fields (PDF). *NMR Biomed.* 2011; 24(9): 1129–1136.
89. de Rochefort L, Liu T, Kressler B, Liu J, Spincemaille P, Lebon V, Wu J, Wang Y. Quantitative susceptibility map reconstruction from MR phase data using bayesian regularization: validation and application to brain imaging. *Magn. Reson. Med.* 2010; 63(1): 194–206.
90. Zhou D, Liu T, Spincemaille P, Wang Y. Background field removal by solving the Laplacian boundary value problem. *NMR Biomed.* 2014; 27(3): 312–319.
91. Wharton S, Schafer A, Bowtell R. Susceptibility mapping in the human brain using threshold-based k-space division. *Magn. Reson. Med.* 2010; 63(5): 1292–1304.
92. Schweser F, Sommer K, Atterbury M, Deistung A, Lehr BW, Reichenbach JR. On the impact of regularization and kernel type on SHARP-corrected GRE phase images. *Proceedings of the 19th Annual Meeting ISMRM, Montreal, QC, Canada, 2011*; 2667.
93. Sun H, Wilman AH. Background field removal using spherical mean value filtering and Tikhonov regularization. *Magn. Reson. Med.* 2014; 71(3): 1151–1157.
94. Wu B, Li W, Guidon A, Liu C. Whole brain susceptibility mapping using compressed sensing. *Magn. Reson. Med.* 2012; 67(1): 137–147.
95. Schweser F, Deistung A, Sommer K, Reichenbach JR. Toward online reconstruction of quantitative susceptibility maps: superfast dipole inversion. *Magn. Reson. Med.* 2013; 69(6): 1582–1594.
96. Topfer R, Schweser F, Deistung A, Reichenbach JR, Wilman AH. SHARP edges: recovering cortical phase contrast through harmonic extension. *Magn. Reson. Med.* 2015; 73(2): 851–856.
97. Neelavalli J, Cheng YC, Jiang J, Haacke EM. Removing background phase variations in susceptibility-weighted imaging using a fast, forward-field calculation. *J. Magn. Reson. Imaging* 2009; 29(4): 937–948.
98. Shmueli K, de Zwart JA, van Gelderen P, Li TQ, Dodd SJ, Duyn JH. Magnetic susceptibility mapping of brain tissue in vivo using MRI phase data. *Magn. Reson. Med.* 2009; 62(6): 1510–1522.
99. Liu T, Spincemaille P, de Rochefort L, Kressler B, Wang Y. Calculation of susceptibility through multiple orientation sampling (COSMOS): a method for conditioning the inverse problem from measured magnetic field map to susceptibility source image in MRI. *Magn. Reson. Med.* 2009; 61(1): 196–204.
100. Wharton S, Bowtell R. Whole-brain susceptibility mapping at high field: a comparison of multiple- and single-orientation methods. *Neuroimage* 2010; 53(2): 515–525.
101. Schweser F, Sommer K, Deistung A, Reichenbach JR. Quantitative susceptibility mapping for investigating subtle susceptibility variations in the human brain. *Neuroimage* 2012; 62(3): 2083–2100.
102. Bilgic B, Chatnuntawech I, Fan AP, Setsompop K, Cauley SF, Wald LL, Adalsteinsson E. Fast image reconstruction with L2-regularization. *J. Magn. Reson. Imaging* 2014; 40(1): 181–191.
103. Khabipova D, Wiaux Y, Gruetter R, Marques JP. A modulated closed form solution for quantitative susceptibility mapping—a thorough evaluation and comparison to iterative methods based on edge prior knowledge. *Neuroimage* 2015; 107: 163–174.
104. de Rochefort L, Brown R, Prince MR, Wang Y. Quantitative MR susceptibility mapping using piece-wise constant regularized inversion of the magnetic field. *Magn. Reson. Med.* 2008; 60(4): 1003–1009.
105. Kressler B, de Rochefort L, Liu T, Spincemaille P, Jiang Q, Wang Y. Nonlinear regularization for per voxel estimation of magnetic susceptibility distributions from MRI field maps. *IEEE Trans. Med. Imaging* 2010; 29(2): 273–281.
106. Bilgic B, Pfefferbaum A, Rohlfing T, Sullivan EV, Adalsteinsson E. MRI estimates of brain iron concentration in normal aging using quantitative susceptibility mapping. *Neuroimage* 2012; 59(3): 2625–2635.
107. Liu J, Liu T, de Rochefort L, Ledoux J, Khalidov I, Chen W, Tsiouris AJ, Wisnieff C, Spincemaille P, Prince MR, Wang Y. Morphology enabled dipole inversion for quantitative susceptibility mapping using structural consistency between the magnitude image and the susceptibility map. *Neuroimage* 2012; 59(3): 2560–2568.
108. Li W, Wang N, Yu F, Han H, Cao W, Romero R, Tantiwongkosi B, Duong TQ, Liu C. A method for estimating and removing streaking artifacts in quantitative susceptibility mapping. *Neuroimage* 2015; 108: 111–122.
109. Wen Y, Wang Y, Liu T. Enhancing k-space quantitative susceptibility mapping by enforcing consistency on the cone data (CCD) with structural priors. *Magn. Reson. Med.* 2016; 75(2): 823–830.
110. Tang J, Liu S, Neelavalli J, Cheng YC, Buch S, Haacke EM. Improving susceptibility mapping using a threshold-based K-space/image domain iterative reconstruction approach. *Magn. Reson. Med.* 2013; 69(5): 1396–1407.
111. Wei H, Dibb R, Zhou Y, Sun Y, Xu J, Wang N, Liu C. Streaking artifact reduction for quantitative susceptibility mapping of sources with large dynamic range. *NMR Biomed.* 2015; 28(10): 1294–1303.
112. Sun H, Kate M, Gioia LC, Emery DJ, Butcher K, Wilman AH. Quantitative susceptibility mapping using a superposed dipole inversion method: application to intracranial hemorrhage. *Magn. Reson. Med.* 2015 [Epub ahead of print]. DOI:10.1002/mrm.25919.
113. Sharma SD, Hernando D, Horng DE, Reeder SB. Quantitative susceptibility mapping in the abdomen as an imaging biomarker of hepatic iron overload. *Magn. Reson. Med.* 2015; 74(3): 673–683.
114. Dong J, Liu T, Chen F, Zhou D, Dimov A, Raj A, Cheng Q, Spincemaille P, Wang Y. Simultaneous phase unwrapping and removal of chemical shift (SPURS) using graph cuts: application in quantitative susceptibility mapping. *IEEE Trans. Med. Imaging* 2015; 34(2): 531–540.
115. Li X, Vikram DS, Lim IA, Jones CK, Farrell JA, van Zijl PC. Mapping magnetic susceptibility anisotropies of white matter in vivo in the human brain at 7 T. *Neuroimage* 2012; 62(1): 314–330.
116. Wisnieff C, Liu T, Spincemaille P, Wang S, Zhou D, Wang Y. Magnetic susceptibility anisotropy: cylindrical symmetry from macroscopically ordered anisotropic molecules and accuracy of MRI measurements using few orientations. *Neuroimage* 2013; 70: 363–376.
117. Lee J, Shmueli K, Fukunaga M, van Gelderen P, Merkle H, Silva AC, Duyn JH. Sensitivity of MRI resonance frequency to the orientation of brain tissue microstructure. *Proc. Natl. Acad. Sci. U. S. A.* 2010; 107(11): 5130–5135.
118. Xie L, Dibb R, Cofer GP, Li W, Nicholls PJ, Johnson GA, Liu C. Susceptibility tensor imaging of the kidney and its microstructural underpinnings. *Magn. Reson. Med.* 2015; 73(3): 1270–1281.
119. Li X, van Zijl PC. Mean magnetic susceptibility regularized susceptibility tensor imaging (MMSR-STI) for estimating orientations of white matter fibers in human brain. *Magn. Reson. Med.* 2014; 72(3): 610–619.
120. Liu C, Murphy NE, Li W. Probing white-matter microstructure with higher-order diffusion tensors and susceptibility tensor MRI. *Front. Integr. Neurosci.* 2013; 7: 11.
121. Li W, Liu C. Comparison of magnetic susceptibility tensor and diffusion tensor of the brain. *J. Neurosci. Neuroeng.* 2013; 2(5): 431–440.
122. Le Bihan D, Mangin JF, Poupon C, Clark CA, Pappata S, Molko N, Chabriat H. Diffusion tensor imaging: concepts and applications. *J. Magn. Reson. Imaging* 2001; 13(4): 534–546.
123. He X, Yablonskiy DA. Biophysical mechanisms of phase contrast in gradient echo MRI. *Proc. Natl. Acad. Sci. U. S. A.* 2009; 106(32): 13 558–13 563.
124. Ye FQ, Allen PS. Relaxation enhancement of the transverse magnetization of water protons in paramagnetic suspensions of red blood cells. *Magn. Reson. Med.* 1995; 34(5): 713–720.
125. Wolber J, Cherubini A, Leach MO, Bifone A. Hyperpolarized ¹²⁹Xe NMR as a probe for blood oxygenation. *Magn. Reson. Med.* 2000; 43(4): 491–496.
126. Boesch C, Slotboom J, Hoppeler H, Kreis R. In vivo determination of intra-myocellular lipids in human muscle by means of localized ¹H-MR-spectroscopy. *Magn. Reson. Med.* 1997; 37(4): 484–493.
127. Luo J, He X, Yablonskiy DA. Magnetic susceptibility induced white matter MR signal frequency shifts—experimental comparison between Lorentzian sphere and generalized Lorentzian approaches. *Magn. Reson. Med.* 2014; 71(3): 1251–1263.
128. Wharton S, Bowtell R. Effects of white matter microstructure on phase and susceptibility maps. *Magn. Reson. Med.* 2015; 73(3): 1258–1269.

129. Yablonskiy DA, Sukstanskii AL. Generalized Lorentzian Tensor Approach (GLTA) as a biophysical background for quantitative susceptibility mapping. *Magn. Reson. Med.* 2015; 73(2): 757–764.
130. Hopkins JA, Wehrli FW. Magnetic susceptibility measurement of insoluble solids by NMR: magnetic susceptibility of bone. *Magn. Reson. Med.* 1997; 37(4): 494–500.
131. Kawamura Y, Sakurai I, Ikegami A, Iwayanagi S. Magneto-orientation of phospholipids. *Mol. Cryst. Liq. Cryst.* 1981; 67(1–4): 733–743.
132. Stoffel W. The function of oligodendrocytes in the maturation of the brain. In *Cellular Metabolism of the Arterial Wall and Central Nervous System: Selected Aspects*, Schettler G, Greten H, Habenicht AJR (eds). Springer: Berlin, Heidelberg, 2012, pp. 55–76.
133. Liu C, Li W, Johnson GA, Wu B. High-field (9.4 T) MRI of brain demyelination by quantitative mapping of magnetic susceptibility. *Neuroimage* 2011; 56(3): 930–938.
134. van Gelderen P, Mandelkowitz H, de Zwart JA, Duyn JH. A torque balance measurement of anisotropy of the magnetic susceptibility in white matter. *Magn. Reson. Med.* 2015; 74(5): 1388–1396.
135. Haacke EM, Cheng NY, House MJ, Liu Q, Neelavalli J, Ogg RJ, Khan A, Ayaz M, Kirsch W, Obenaus A. Imaging iron stores in the brain using magnetic resonance imaging. *Magn. Reson. Imaging* 2005; 23(1): 1–25.
136. Beard JL, Connor JR, Jones BC. Iron in the brain. *Nutr. Rev.* 1993; 51(6): 157–170.
137. Hadzhiyeva M, Kirches E, Mawrin C. Review: iron metabolism and the role of iron in neurodegenerative disorders. *Neuropathol. Appl. Neurobiol.* 2014; 40(3): 240–257.
138. Ward RJ, Zucca FA, Duyn JH, Crichton RR, Zecca L. The role of iron in brain ageing and neurodegenerative disorders. *Lancet Neurol.* 2014; 13(10): 1045–1060.
139. Ramos P, Santos A, Pinto NR, Mendes R, Magalhaes T, Almeida A. Iron levels in the human brain: a post-mortem study of anatomical region differences and age-related changes. *J. Trace Elem. Med. Biol.* 2014; 28(1): 13–17.
140. Hallgren B, Sourander P. The effect of age on the non-haem iron in the human brain. *J. Neurochem.* 1958; 3(1): 41–51.
141. Hebbrecht G, Maenhaut W, De Reuck J. Brain trace elements and aging. *Nucl. Instrum. Methods B* 1999; 150(1–4): 208–213.
142. Li W, Wu B, Batrachenko A, Bancroft-Wu V, Morey RA, Shashi V, Langhammer C, De Bellis MD, Ropele S, Song AW, Liu C. Differential developmental trajectories of magnetic susceptibility in human brain gray and white matter over the lifespan. *Hum. Brain Mapp.* 2014; 35(6): 2698–2713.
143. Persson N, Wu J, Zhang Q, Liu T, Shen J, Bao R, Ni M, Liu T, Wang Y, Spincemille P. Age and sex related differences in subcortical brain iron concentrations among healthy adults. *Neuroimage* 2015; 122: 385–398.
144. Spees WM, Yablonskiy DA, Oswood MC, Ackerman JJH. Water proton MR properties of human blood at 1.5 Tesla: magnetic susceptibility, T₁, T₂, T₂^{*}, and non-Lorentzian signal behavior. *Magn. Reson. Med.* 2001; 45: 533–542.
145. Neelavalli J, Cheng YC. Magnetic Susceptibility. In *MRI Susceptibility Weighted Imaging: Basic Concepts and Clinical Applications*. Haacke EM, Reichenbach JR, Xu Y (eds). John Wiley & Sons: Hoboken, New Jersey, 2011; pp. 17–31.
146. Haacke EM, Lai S, Reichenbach JR, Kuppusamy K, Hoogenraad FG, Takeichi H, Lin W. In vivo measurement of blood oxygen saturation using magnetic resonance imaging: a direct validation of the blood oxygen level-dependent concept in functional brain imaging. *Hum. Brain Mapp.* 1997; 5(5): 341–346.
147. Silbernagl S, Despopoulos A. *Taschenatlas der Physiologie*, 5th edn. Stuttgart: Georg Thieme Verlag, 2001, p. 88.
148. Weisskoff RM, Kiihne S. MRI susceptometry: image-based measurements of absolute susceptibility of MR contrast agents and human blood. *Magn. Reson. Med.* 1992; 24: 375–383.
149. Thulborn KR, Waterton JC, Matthews PM. Oxygenation dependence of the transverse relaxation time of water protons in whole blood at high field. *Biochim. Biophys. Acta* 1982; 714: 265–270.
150. Jain V, Abdulmalik O, Proppert KJ, Wehrli FW. Investigating the magnetic susceptibility properties of fresh human blood for noninvasive oxygen saturation quantification. *Magn. Reson. Med.* 2012; 68(3): 863–867.
151. Haacke EM, Reichenbach JR, Xu Y. *Susceptibility Weighted Imaging in MRI: Basic Concepts and Clinical Applications*. John Wiley & Sons: Hoboken, New Jersey, 2011.
152. He N, Ling H, Ding B, Huang J, Zhang Y, Zhang Z, Liu C, Chen K, Yan F. Region-specific disturbed iron distribution in early idiopathic Parkinson's disease measured by quantitative susceptibility mapping. *Hum. Brain Mapp.* 2015; 36(11): 4407–4420.
153. Deistung A, Schweser F, Wiestler B, Abello M, Roethke M, Sahm F, Wick W, Nagel AM, Heiland S, Schlemmer HP, Bendszus M, Reichenbach JR, Radbruch A. Quantitative susceptibility mapping differentiates between blood depositions and calcifications in patients with glioblastoma. *PLoS One* 2013; 8(3): e57924.
154. Barbosa JH, Santos AC, Tumas V, Liu M, Zheng W, Haacke EM, Salmon CE. Quantifying brain iron deposition in patients with Parkinson's disease using quantitative susceptibility mapping, R₂ and R₂^{*}. *Magn. Reson. Imaging* 2015; 33(5): 559–565.
155. Liu T, Eskreis-Winkler S, Schweitzer AD, Chen W, Kaplitt MG, Tsiouris AJ, Wang Y. Improved subthalamic nucleus depiction with quantitative susceptibility mapping. *Radiology* 2013; 269(1): 216–223.
156. Fernandez-Seara MA, Wehrli FW. Postprocessing technique to correct for background gradients in image-based R₂(2) measurements. *Magn. Reson. Med.* 2000; 44(3): 358–366.
157. Schäfer A, Wharton S, Gowland P, Bowtell R. Using magnetic field simulation to study susceptibility-related phase contrast in gradient echo MRI. *Neuroimage* 2009; 48(1): 126–137.
158. Deistung A, Schäfer A, Schweser F, Biedermann U, Turner R, Reichenbach JR. Toward in vivo histology: a comparison of quantitative susceptibility mapping (QSM) with magnitude-, phase-, and R₂^{*}-imaging at ultra-high magnetic field strength. *Neuroimage* 2013; 65: 299–314.
159. Deistung A, Schäfer A, Schweser F, Biedermann U, Gullmar D, Trampel R, Turner R, Reichenbach JR. High-resolution MR imaging of the human brainstem in vivo at 7 Tesla. *Front. Hum. Neurosci.* 2013; 7: 710.
160. Schneider TM, Deistung A, Biedermann U, Matthies C, Ernestus R-I, Volkmann J, Heiland S, Bendszus M, Reichenbach JR. Susceptibility Sensitive Magnetic Resonance Imaging Displays Pallidofugal and Striatonigral Fiber Tracts. *Operative Neurosurgery* DOI:10.1227/NEU.0000000000001256.
161. Chandran AS, Bynevelt M, Lind CR. Magnetic resonance imaging of the subthalamic nucleus for deep brain stimulation. *J. Neurosurg.* 2016; 124(1): 96–105.
162. Ashkan K, Blomstedt P, Zrinzo L, Tisch S, Yousry T, Limousin-Dowsey P, Hariz MI. Variability of the subthalamic nucleus: the case for direct MRI guided targeting. *Br. J. Neurosurg.* 2007; 21(2): 197–200.
163. Deistung A, Schäfer A, Schweser F, Reichenbach JR. Cortical mapping of magnetic susceptibility and R₂^{*} reveals insights into tissue composition. *Proceedings of the 23rd Annual Meeting ISMRM*, Toronto, ON, Canada, 2015; 284.
164. Khabipova D, Gruetter R, Marques JP. Human cortical surface maps of three quantitative imaging parameters: R₁, R₂^{*} and magnetic susceptibility. *Proceedings of the 23rd Annual Meeting ISMRM*, Toronto, ON, Canada, 2015; 929.
165. Fukunaga M, Li TQ, van Gelderen P, de Zwart JA, Shmueli K, Yao B, Lee J, Maric D, Aronova MA, Zhang G, Leapman RD, Schenck JF, Merkle H, Duyn JH. Layer-specific variation of iron content in cerebral cortex as a source of MRI contrast. *Proc. Natl. Acad. Sci. U. S. A.* 2010; 107(8): 3834–3839.
166. Deistung A, Stefanescu MR, Ernst TM, Schlamann M, Ladd ME, Reichenbach JR, Timmann D. Structural and functional magnetic resonance imaging of the cerebellum: considerations for assessing cerebellar ataxias. *Cerebellum* 2016; 15(1): 21–25.
167. Kornienko VN, Pronin IN. *Diagnostic Neuroradiology*. Springer-Verlag: Berlin, Heidelberg, 2009.
168. Chen W, Zhu W, Kovanlikaya I, Kovanlikaya A, Liu T, Wang S, Salustri C, Wang Y. Intracranial calcifications and hemorrhages: characterization with quantitative susceptibility mapping. *Radiology* 2014; 270(2): 496–505.
169. Liu J, Xia S, Hanks R, Wiseman N, Peng C, Zhou S, Haacke EM, Kou Z. Susceptibility weighted imaging and mapping of micro-hemorrhages and major deep veins after traumatic brain injury. *J. Neurotrauma* 2016; 33(1): 10–21.
170. Huang YL, Kuo YS, Tseng YC, Chen DY, Chiu WT, Chen CJ. Susceptibility-weighted MRI in mild traumatic brain injury. *Neurology* 2015; 84(6): 580–585.
171. Babikian T, Freier MC, Tong KA, Nickerson JP, Wall CJ, Holshouser BA, Burley T, Riggs ML, Ashwal S. Susceptibility

- weighted imaging: neuropsychologic outcome and pediatric head injury. *Pediatr. Neurol.* 2005; 33(3): 184–194.
172. Shoamanesh A, Kwok CS, Benavente O. Cerebral microbleeds: histopathological correlation of neuroimaging. *Cerebrovasc. Dis.* 2011; 32(6): 528–534.
173. Tong KA, Ashwal S, Holshouser BA, Shutter LA, Herigault G, Haacke EM, Kido DK. Hemorrhagic shearing lesions in children and adolescents with posttraumatic diffuse axonal injury: improved detection and initial results. *Radiology* 2003; 227(2): 332–339.
174. Tong KA, Ashwal S, Holshouser BA, Nickerson JP, Wall CJ, Shutter LA, Osterdock RJ, Haacke EM, Kido D. Diffuse axonal injury in children: clinical correlation with hemorrhagic lesions. *Ann. Neurol.* 2004; 56(1): 36–50.
175. Liu W, Soderlund K, Senseney JS, Joy D, Yeh PH, Ollinger J, Sham EB, Liu T, Wang Y, Oakes TR, Riedy G. Imaging cerebral microhemorrhages in military service members with chronic traumatic brain injury. *Radiology* 2016; 278(2): 536–545.
176. Cervos-Navarro J, Lafuente JV. Traumatic brain injuries: structural changes. *J. Neurol. Sci.* 1991; 103(Suppl): S3–S14.
177. Weisberg LA, Garcia C, Strub C. Head Trauma. In: *Essentials of Clinical Neurology* Mosby: St. Louis; 1996; 356–380.
178. Lobel U, Sedlacik J, Sabin ND, Kocak M, Broniscer A, Hillenbrand CM, Patay Z. Three-dimensional susceptibility-weighted imaging and two-dimensional T2*-weighted gradient-echo imaging of intratumoral hemorrhages in pediatric diffuse intrinsic pontine glioma. *Neuroradiology* 2010; 52(12): 1167–1177.
179. Louis DN, Ohgaki H, Wiestler OD, Cavenee WK. *World Health Organization Classification of Tumours of the Central Nervous System*. World Health Organization: Lyon, 2007.
180. Sehgal V, Delproposto Z, Haddad D, Haacke EM, Sloan AE, Zamorano LJ, Barger G, Hu J, Xu Y, Prabhakaran KP, Elangovan IR, Neelavalli J, Reichenbach JR. Susceptibility-weighted imaging to visualize blood products and improve tumor contrast in the study of brain masses. *J. Magn. Reson. Imaging* 2006; 24(1): 41–51.
181. Bahr O, Hattungen E, Rieger J, Steinbach JP. Bevacizumab-induced tumor calcifications as a surrogate marker of outcome in patients with glioblastoma. *Neuro Oncol.* 2011; 13(9): 1020–1029.
182. Braak H, Del Tredici K, Rub U, de Vos RA, Jansen Steur EN, Braak E. Staging of brain pathology related to sporadic Parkinson's disease. *Neurobiol. Aging* 2003; 24(2): 197–211.
183. Damier P, Hirsch EC, Agid Y, Graybiel AM. The substantia nigra of the human brain. II. Patterns of loss of dopamine-containing neurons in Parkinson's disease. *Brain* 1999; 122(Pt 8): 1437–1448.
184. Berg D, Godau J, Walter U. Transcranial sonography in movement disorders. *Lancet Neurol.* 2008; 7(11): 1044–1055.
185. Mahlknecht P, Seppi K, Stockner H, Nocker M, Scherfler C, Kiechl S, Willeit J, Schmidauer C, Gasperi A, Rungger G, Poewe W. Substantia nigra hyperechogenicity as a marker for Parkinson's disease: a population-based study. *Neurodegener Dis* 2013; 12(4): 212–218.
186. Berg D, Roggendorf W, Schroder U, Klein R, Tatschner T, Benz P, Tucha O, Preier M, Lange KW, Reiners K, Gerlach M, Becker G. Echogenicity of the substantia nigra: association with increased iron content and marker for susceptibility to nigrostriatal injury. *Arch. Neurol.* 2002; 59(6): 999–1005.
187. Dexter DT, Carayon A, Javoy-Agid F, Agid Y, Wells FR, Daniel SE, Lees AJ, Jenner P, Marsden CD. Alterations in the levels of iron, ferritin and other trace metals in Parkinson's disease and other neurodegenerative diseases affecting the basal ganglia. *Brain* 1991; 114(Pt 4): 1953–1975.
188. Murakami Y, Kakeda S, Watanabe K, Ueda I, Ogasawara A, Moriya J, Ide S, Futatsuya K, Sato T, Okada K, Uozumi T, Tsuji S, Liu T, Wang Y, Korogi Y. Usefulness of quantitative susceptibility mapping for the diagnosis of Parkinson disease. *Am. J. Neuroradiol.* 2015; 36(6): 1102–1108.
189. Lotfipour AK, Wharton S, Schwarz ST, Gontu V, Schafer A, Peters AM, Bowtell RW, Auer DP, Gowland PA, Bajaj NP. High resolution magnetic susceptibility mapping of the substantia nigra in Parkinson's disease. *J. Magn. Reson. Imaging* 2012; 35(1): 48–55.
190. Blazejewska AI, Schwarz ST, Pitiot A, Stephenson MC, Lowe J, Bajaj N, Bowtell RW, Auer DP, Gowland PA. Visualization of nigrosome 1 and its loss in PD: pathoanatomical correlation and in vivo 7 T MRI. *Neurology* 2013; 81(6): 534–540.
191. Hallgren B, Sourander P. The non-haemin iron in the cerebral cortex in Alzheimer's disease. *J. Neurochem.* 1960; 5: 307–310.
192. LeVine SM. Iron deposits in multiple sclerosis and Alzheimer's disease brains. *Brain Res.* 1997; 760(1–2): 298–303.
193. Smith MA, Zhu X, Tabaton M, Liu G, McKeel DW, Jr, Cohen ML, Wang X, Siedlak SL, Dwyer BE, Hayashi T, Nakamura M, Nunomura A, Perry G. Increased iron and free radical generation in preclinical Alzheimer disease and mild cognitive impairment. *J. Alzheimers Dis.* 2010; 19(1): 363–372.
194. Good PF, Perl DP, Bierer LM, Schmeidler J. Selective accumulation of aluminum and iron in the neurofibrillary tangles of Alzheimer's disease: a laser microprobe (LAMMA) study. *Ann. Neurol.* 1992; 31(3): 286–292.
195. Schubert D, Chevion M. The role of iron in beta amyloid toxicity. *Biochem. Biophys. Res. Commun.* 1995; 216(2): 702–707.
196. Leskovjan AC, Kretlow A, Lanzitotti A, Barrea R, Vogt S, Miller LM. Increased brain iron coincides with early amyloid formation in a mouse model of Alzheimer's disease. *Neuroimage* 2011; 55(1): 32–38.
197. Acosta-Cabrero J, Williams GB, Cardenas-Blanco A, Arnold RJ, Lupson V, Nestor PJ. In vivo quantitative susceptibility mapping (QSM) in Alzheimer's disease. *PLoS One* 2013; 8(11): e81093.
198. Moon Y, Han SH, Moon WJ. Patterns of brain iron accumulation in vascular dementia and Alzheimer's dementia using quantitative susceptibility mapping imaging. *J. Alzheimers Dis.* 2016; 51(3): 737–745.
199. Schäfer A, Tiepolt S, Roggenhofer E, Trampel R, Stueber C, Zeisig V, Grossmann U, Jochimsen TH, Sabri O, Turner R, Barthel H. Quantitative susceptibility mapping (QSM) in β -amyloid-PET-confirmed Alzheimer's disease at 7 T. Proceedings of the 22nd Annual Meeting ISMRM, Milan, Italy, 2014; 3267.
200. Wengenack TM, Reyes DA, Curran GL, Borowski BJ, Lin J, Preboske GM, Holasek SS, Gilles EJ, Chamberlain R, Marjanska M, Jack CR, Jr, Garwood M, Poduslo JF. Regional differences in MRI detection of amyloid plaques in AD transgenic mouse brain. *Neuroimage* 2011; 54(1): 113–122.
201. Nakada T, Matsuzawa H, Igarashi H, Fujii Y, Kwee IL. In vivo visualization of senile-plaque-like pathology in Alzheimer's disease patients by MR microscopy on a 7 T system. *J. Neuroimaging* 2008; 18(2): 125–129.
202. Kidd D, Barkhof F, McConnell R, Algra PR, Allen IV, Revesz T. Cortical lesions in multiple sclerosis. *Brain* 1999; 122(Pt 1): 17–26.
203. Compston A, Coles A. Multiple sclerosis. *Lancet* 2008; 372(9648): 1502–1517.
204. Langkammer C, Liu T, Khalil M, Enzinger C, Jehna M, Fuchs S, Fazekas F, Wang Y, Ropele S. Quantitative susceptibility mapping in multiple sclerosis. *Radiology* 2013; 267(2): 551–559.
205. Rudko DA, Solovey I, Gati JS, Kremenchutzky M, Menon RS. Multiple sclerosis: improved identification of disease-relevant changes in gray and white matter by using susceptibility-based MR imaging. *Radiology* 2014; 272(3): 851–864.
206. Cobzas D, Sun H, Walsh AJ, Lebel RM, Blevins G, Wilman AH. Subcortical gray matter segmentation and voxel-based analysis using transverse relaxation and quantitative susceptibility mapping with application to multiple sclerosis. *J. Magn. Reson. Imaging* 2015; 42(6): 1601–1610.
207. Blazejewska AI, Al-Radaideh AM, Wharton S, Lim SY, Bowtell RW, Constantinescu CS, Gowland PA. Increase in the iron content of the substantia nigra and red nucleus in multiple sclerosis and clinically isolated syndrome: a 7 Tesla MRI study. *J. Magn. Reson. Imaging* 2015; 41(4): 1065–1070.
208. Hammond KE, Metcalf M, Carvajal L, Okuda DT, Srinivasan R, Vigneron D, Nelson SJ, Pelletier D. Quantitative in vivo magnetic resonance imaging of multiple sclerosis at 7 Tesla with sensitivity to iron. *Ann. Neurol.* 2008; 64(6): 707–713.
209. Bagnato F, Hametner S, Yao B, van Gelderen P, Merkle H, Cantor FK, Lassmann H, Duyn JH. Tracking iron in multiple sclerosis: a combined imaging and histopathological study at 7 Tesla. *Brain* 2011; 134(Pt 12): 3602–3615.
210. Li X, Harrison DM, Liu H, Jones CK, Oh J, Calabresi PA, van Zijl PC. Magnetic susceptibility contrast variations in multiple sclerosis lesions. *J. Magn. Reson. Imaging* 2016; 43(2): 463–473.
211. Wisnieff C, Ramanan S, Olesik J, Gauthier S, Wang Y, Pitt D. Quantitative susceptibility mapping (QSM) of white matter multiple sclerosis lesions: interpreting positive susceptibility and the presence of iron. *Magn. Reson. Med.* 2015; 74(2): 564–570.

212. Chen W, Gauthier SA, Gupta A, Comunale J, Liu T, Wang S, Pei M, Pitt D, Wang Y. Quantitative susceptibility mapping of multiple sclerosis lesions at various ages. *Radiology* 2014; 271(1): 183–192.
213. Hametner S, Wimmer I, Haider L, Pfeifenbring S, Bruck W, Lassmann H. Iron and neurodegeneration in the multiple sclerosis brain. *Ann. Neurol.* 2013; 74(6): 848–861.
214. Yablonskiy DA, Luo J, Sukstanskii AL, Iyer A, Cross AH. Biophysical mechanisms of MRI signal frequency contrast in multiple sclerosis. *Proc. Natl. Acad. Sci.* 2012; 109(35): 14 212–14 217.USA
215. Klockgether T. Update on degenerative ataxias. *Curr. Opin. Neurol.* 2011; 24(4): 339–345.
216. Koeppen AH, Kuntzsch EC, Bjork ST, Ramirez RL, Mazurkiewicz JE, Feustel PJ. Friedreich ataxia: metal dysmetabolism in dorsal root ganglia. *Acta Neuropathol. Commun.* 2013; 1(1): 26.
217. Koeppen AH, Michael SC, Knutson MD, Haile DJ, Qian J, Levi S, Santambrogio P, Garrick MD, Lamarche JB. The dentate nucleus in Friedreich's ataxia: the role of iron-responsive proteins. *Acta Neuropathol.* 2007; 114(2): 163–173.
218. Donato SD, Mariotti C, Taroni F. Chapter 25 – Spinocerebellar ataxia type 1. In *Handbook of Clinical Neurology*, Sankara HS, Alexandra D (eds), Vol. 103. Elsevier: Amsterdam, 2012, pp. 399–421.
219. Gierga K, Schelhaas HJ, Brunt ER, Seidel K, Scherzed W, Egensperger R, de Vos RA, den Dunnen W, Ippel PF, Petrasch-Parwez E, Deller T, Schols L, Rub U. Spinocerebellar ataxia type 6 (SCA6): neurodegeneration goes beyond the known brain predilection sites. *Neuropathol. Appl. Neurobiol.* 2009; 35(5): 515–527.
220. Koeppen AH, Ramirez RL, Yu D, Collins SE, Qian J, Parsons PJ, Yang KX, Chen Z, Mazurkiewicz JE, Feustel PJ. Friedreich's ataxia causes redistribution of iron, copper, and zinc in the dentate nucleus. *Cerebellum* 2012; 11(4): 845–860.
221. Diedrichsen J, Maderwald S, Kuper M, Thurling M, Rabe K, Gizewski ER, Ladd ME, Timmann D. Imaging the deep cerebellar nuclei: a probabilistic atlas and normalization procedure. *Neuroimage* 2011; 54(3): 1786–1794.
222. Maderwald S, Thurling M, Kuper M, Theysohn N, Muller O, Beck A, Aurich V, Ladd ME, Timmann D. Direct visualization of cerebellar nuclei in patients with focal cerebellar lesions and its application for lesion-symptom mapping. *Neuroimage* 2012; 63(3): 1421–1431.
223. Stefanescu MR, Dohnalek M, Maderwald S, Thurling M, Minnerop M, Beck A, Schlamann M, Diedrichsen J, Ladd ME, Timmann D. Structural and functional MRI abnormalities of cerebellar cortex and nuclei in SCA3, SCA6 and Friedreich's ataxia. *Brain* 2015; 138(Pt 5): 1182–1197.
224. Bonilha da Silva C, Bergo FP, D'Abreu A, Cendes F, Lopes-Cendes I, Franca MC, Jr. Dentate nuclei T2 relaxometry is a reliable neuroimaging marker in Friedreich's ataxia. *Eur. J. Neurol.* 2014; 21(8): 1131–1136.
225. Solbach K, Kraff O, Minnerop M, Beck A, Schols L, Gizewski ER, Ladd ME, Timmann D. Cerebellar pathology in Friedreich's ataxia: atrophied dentate nuclei with normal iron content. *Neurol. Clin.* 2014; 6: 93–99.
226. Waldvogel D, van Gelderen P, Hallett M. Increased iron in the dentate nucleus of patients with Friedrich's ataxia. *Ann. Neurol.* 1999; 46(1): 123–125.
227. Boddaert N, Le Quan Sang KH, Rotig A, Leroy-Willig A, Gallet S, Brunelle F, Sidi D, Thalabard JC, Munnich A, Cabantchik ZI. Selective iron chelation in Friedreich ataxia: biologic and clinical implications. *Blood* 2007; 110(1): 401–408.
228. Schafer A, Forstmann BU, Neumann J, Wharton S, Mietke A, Bowtell R, Turner R. Direct visualization of the subthalamic nucleus and its iron distribution using high-resolution susceptibility mapping. *Hum. Brain Mapp.* 2012; 33(12): 2831–2842.
229. Perlmuter JS, Mink JW. Deep brain stimulation. *Annu. Rev. Neurosci.* 2006; 29: 229–257.
230. Patel NK, Khan S, Gill SS. Comparison of atlas- and magnetic-resonance-imaging-based stereotactic targeting of the subthalamic nucleus in the surgical treatment of Parkinson's disease. *Stereotact. Funct. Neurosurg.* 2008; 86(3): 153–161.
231. Brittenham GM, Farrell DE, Harris JW, Feldman ES, Danish EH, Muir WA, Tripp JH, Bellon EM. Magnetic-susceptibility measurement of human iron stores. *N. Engl. J. Med.* 1982; 307(27): 1671–1675.
232. Hankins JS, McCarville MB, Loeffler RB, Smeltzer MP, Onciu M, Hoffer FA, Li CS, Wang WC, Ware RE, Hillenbrand CM. R2* magnetic resonance imaging of the liver in patients with iron overload. *Blood* 2009; 113(20): 4853–4855.
233. Wood JC, Enriquez C, Ghugre N, Tyzka JM, Carson S, Nelson MD, Coates TD. MRI R2 and R2* mapping accurately estimates hepatic iron concentration in transfusion-dependent thalassemia and sickle cell disease patients. *Blood* 2005; 106(4): 1460–1465.
234. St Pierre TG, Clark PR, Chua-Anusorn W. Single spin-echo proton transverse relaxometry of iron-loaded liver. *NMR Biomed.* 2004; 17(7): 446–458.
235. Anderson LJ, Holden S, Davis B, Prescott E, Charrier CC, Bunce NH, Firmin DN, Wonke B, Porter J, Walker JM, Pennell DJ. Cardiovascular T2-star (T2*) magnetic resonance for the early diagnosis of myocardial iron overload. *Eur. Heart J.* 2001; 22(23): 2171–2179.
236. Straub S, Röthke MC, Schlemmer H-P, Ladd ME, Jobke B, Laun FB. Prostate imaging with quantitative susceptibility mapping (QSM): calcifications. 32nd Annual Scientific Meeting ESMRMB, Edinburgh, UK. Springer: Berlin, Heidelberg; 2015, pp. 178–179.
237. Bai Y, Wang MY, Han YH, Dou SW, Lin Q, Guo Y, Li W, Ding DG, Dai JP, Qin W, Shi DP, Tian J, Dai YM. Susceptibility weighted imaging: a new tool in the diagnosis of prostate cancer and detection of prostatic calcification. *PLoS One* 2013; 8(1): e53237.
238. Schweser F, Herrmann K-H, Deistung A, Atterbury M, Baltzer PAT, Burmeister HP, Kaiser WA, Reichenbach JR. Quantitative magnetic susceptibility mapping (QSM) in breast disease reveals additional information for MR-based characterization of carcinoma and calcification. Proceedings of the 19th Annual Meeting ISMRM, Montreal, QC, Canada, 2011; 1014.
239. Tan H, Thacker J, Liu T, Wang Y, Prasad PV. Feasibility of in vivo quantitative susceptibility mapping in the kidneys. 2nd Workshop on MRI Phase Contrast & Quantitative Susceptibility Mapping (QSM), Ithaca, NY, USA, 2013; 110–113.
240. Wei H, Wang B, Zong X, Lin W, Wang N, Liu C. Imaging magnetic susceptibility of the human knee joint at 3 and 7 Tesla. Proceedings of the 23rd Annual Meeting ISMRM, Toronto, ON, Canada, 2015; 288.
241. Schweser F, Deistung A, Lehr BW, Sommer K, Reichenbach JR. SEMI-TwInS: simultaneous extraction of myelin and iron using a T2*-weighted imaging sequence. Proceedings of the 19th Annual Meeting ISMRM, Montreal, QC, Canada, 2011; 120.
242. Schweser F, Deistung A, Sommer K, Reichenbach JR. Disentangling contributions from iron and myelin architecture to brain tissue magnetic susceptibility by using Quantitative Susceptibility Mapping (QSM). Proceedings of the 20th Annual Meeting ISMRM, Melbourne, Australia, 2012; 409.
243. Stuber C, Morawski M, Schafer A, Labadie C, Wahnert M, Leuze C, Streicher M, Barapatre N, Reimann K, Geyer S, Spemann D, Turner R. Myelin and iron concentration in the human brain: a quantitative study of MRI contrast. *Neuroimage* 2014; 93(Pt 1): 95–106.
244. Terreno E, Geninatti C, Belfiore S, Biancone L, Cabella C, Esposito G, Manazza AD, Aime S. Effect of the intracellular localization of a Gd-based imaging probe on the relaxation enhancement of water protons. *Magn. Reson. Med.* 2006; 55(3): 491–497.
245. Bowen CV, Zhang X, Saab G, Gareau PJ, Rutt BK. Application of the static dephasing regime theory to superparamagnetic iron-oxide loaded cells. *Magn. Reson. Med.* 2002; 48(1): 52–61.
246. Kiselev VG. On the theoretical basis of perfusion measurements by dynamic susceptibility contrast MRI. *Magn. Reson. Med.* 2001; 46(6): 1113–1122.
247. Bonekamp D, Barker PB, Leigh R, van Zijl PC, Li X. Susceptibility-based analysis of dynamic gadolinium bolus perfusion MRI. *Magn. Reson. Med.* 2015; 73(2): 544–554.
248. Xu B, Spincemaille P, Liu T, Prince MR, Dutruel S, Gupta A, Thimmappa ND, Wang Y. Quantification of cerebral perfusion using dynamic quantitative susceptibility mapping. *Magn. Reson. Med.* 2015; 73(4): 1540–1548.
249. Wong R, Chen X, Wang Y, Hu X, Jin MM. Visualizing and quantifying acute inflammation using ICAM-1 specific nanoparticles and MRI quantitative susceptibility mapping. *Ann. Biomed. Eng.* 2012; 40(6): 1328–1338.
250. Klohs J, Deistung A, Ielacqua GD, Seuwen A, Kindler D, Schweser F, Vaas M, Kipar A, Reichenbach JR, Rudin M. Quantitative assessment of microvasculopathy in arcAβ mice with USPIO-enhanced gradient echo MRI. *J. Cereb. Blood Flow Metab.* 2015. [Epub ahead of print]. DOI: 10.1177/0271678X15621500.

251. Di Corato R, Gazeau F, Le Visage C, Fayol D, Levitz P, Lux F, Letourneur D, Luciani N, Tillement O, Wilhelm C. High-resolution cellular MRI: gadolinium and iron oxide nanoparticles for in-depth dual-cell imaging of engineered tissue constructs. *ACS Nano* 2013; 7(9): 7500–7512.
252. Shi H, Liu KJ. Cerebral tissue oxygenation and oxidative brain injury during ischemia and reperfusion. *Front. Biosci.* 2007; 12: 1318–1328.
253. Nordsmark M, Bentzen SM, Rudat V, Brizel D, Lartigau E, Stadler P, Becker A, Adam M, Molls M, Dunst J, Terris DJ, Overgaard J. Prognostic value of tumor oxygenation in 397 head and neck tumors after primary radiation therapy. An international multicenter study. *Radiother. Oncologia* 2005; 77(1): 18–24.
254. Andrews BT, Dujovny M, Mirchandani HG, Ausman JL. Microsurgical anatomy of the venous drainage into the superior sagittal sinus. *Neurosurgery* 1989; 24(4): 514–520.
255. Fan AP, Bilgic B, Gagnon L, Witzel T, Bhat H, Rosen BR, Adalsteinsson E. Quantitative oxygenation venography from MRI phase. *Magn. Reson. Med.* 2014; 72(1): 149–159.
256. Jain V, Magland J, Langham M, Wehrli FW. High temporal resolution in vivo blood oximetry via projection-based T2 measurement. *Magn. Reson. Med.* 2013; 70(3): 785–790.
257. Rodgers ZB, Englund EK, Langham MC, Magland JF, Wehrli FW. Rapid T2- and susceptometry-based CMRO2 quantification with interleaved TRUST (ITRUST). *Neuroimage* 2015; 106: 441–450.
258. Reichenbach JR, Schweser F, Serres B, Deistung A. Quantitative susceptibility mapping: concepts and applications. *Clin. Neuroradiol.* 2015; 25(Suppl. 2): 225–230.
259. Haacke EM, Tang J, Neelavalli J, Cheng YC. Susceptibility mapping as a means to visualize veins and quantify oxygen saturation. *J. Magn. Reson. Imaging* 2010; 32(3): 663–676.
260. Fan AP, Evans KC, Stout JN, Rosen BR, Adalsteinsson E. Regional quantification of cerebral venous oxygenation from MRI susceptibility during hypercapnia. *Neuroimage* 2015; 104: 146–155.
261. Balla DZ, Sanchez-Panchuelo RM, Wharton SJ, Hagberg GE, Scheffler K, Francis ST, Bowtell R. Functional quantitative susceptibility mapping (fQSM). *Neuroimage* 2014; 100: 112–124.
262. Bianciardi M, van Gelderen P, Duyn JH. Investigation of BOLD fMRI resonance frequency shifts and quantitative susceptibility changes at 7 T. *Hum. Brain Mapp.* 2014; 35(5): 2191–2205.
263. Chen Z, Calhoun V. Intrinsic functional brain mapping in reconstructed 4D magnetic susceptibility (chi) data space. *J. Neurosci. Methods* 2015; 241: 85–93.
264. Chen Z, Liu J, Calhoun VD. Susceptibility-based functional brain mapping by 3D deconvolution of an MR-phase activation map. *J. Neurosci. Methods* 2013; 216(1): 33–42.
265. Zhang J, Liu T, Gupta A, Spincemaille P, Nguyen TD, Wang Y. Quantitative mapping of cerebral metabolic rate of oxygen (CMRO2) using quantitative susceptibility mapping (QSM). *Magn. Reson. Med.* 2015; 74(4): 945–952.
266. Klassen L, Menon RS. BOLD signal phase and magnitude dependence on vessel geometry. *Proceedings of the 13th Annual Meeting ISMRM, Miami, FL, USA, 2005*; 496.
267. Wei H, Zhang Y, Gibbs E, Chen NK, Wang N, Liu C. Joint 2D and 3D phase processing for quantitative susceptibility mapping: application to 2D echo-planar imaging. *NMR Biomed.* 2016; [Epub ahead of print]. DOI: 10.1002/nbm.3501.
268. Buch S, Liu S, Ye Y, Cheng YC, Neelavalli J, Haacke EM. Susceptibility mapping of air, bone, and calcium in the head. *Magn. Reson. Med.* 2015; 73(6): 2185–2194.
269. Herrmann KH, Kramer M, Reichenbach JR. Time efficient 3D radial UTE sampling with fully automatic delay compensation on a clinical 3 T MR scanner. *PLoS One* 2016; 11(3): e0150371.
270. He Q, Liu Z, Wang Y, Du J. Ultrashort echo time quantitative susceptibility mapping (UTE-QSM) of cortical bone. *Proceedings of the 23rd Annual Meeting ISMRM, Toronto, ON, Canada, 2015*; 1725.
271. Patenaude B, Smith SM, Kennedy DN, Jenkinson M. A Bayesian model of shape and appearance for subcortical brain segmentation. *Neuroimage* 2011; 56(3): 907–922.
272. Feng X, Deistung A, Schweser F, Güllmar D, Reichenbach JR. Investigation of brain segmentation with FIRST by using different hybrid contrasts and registrations. *Proceedings of the 23rd Annual Meeting ISMRM, Toronto, ON, Canada, 2015*; 3497.
273. Serres B, Deistung A, Schäfer A, Kocinski M, Materka A, Reichenbach JR. Towards characterization of the cerebral venous vessel network using QSM: extraction of vessel radii and lengths. *Proceedings of the 23rd Annual Meeting ISMRM, Toronto, ON, Canada, 2015*; 290.
274. Morris CM, Candy JM, Oakley AE, Bloxham CA, Edwardson JA. Histochemical distribution of non-haem iron in the human brain. *Acta Anat. (Basel)* 1992; 144(3): 235–257.
275. Smith SM. Fast robust automated brain extraction. *Hum. Brain Mapp.* 2002; 17(3): 143–155.
276. Eskildsen SF, Coupe P, Fonov V, Manjon JV, Leung KK, Guizard N, Wassef SN, Ostergaard LR, Collins DL. Alzheimer's disease neuroimaging I. BEaST: brain extraction based on nonlocal segmentation technique. *Neuroimage* 2012; 59(3): 2362–2373.
277. Fischl B, Salat DH, Busa E, Albert M, Dieterich M, Haselgrove C, van der Kouwe A, Killiany R, Kennedy D, Klaveness S, Montillo A, Makris N, Rosen B, Dale AM. Whole brain segmentation: automated labeling of neuroanatomical structures in the human brain. *Neuron* 2002; 33(3): 341–355.
278. Qin L, van Gelderen P, Derbyshire JA, Jin F, Lee J, de Zwart JA, Tao Y, Duyn JH. Prospective head-movement correction for high-resolution MRI using an in-bore optical tracking system. *Magn. Reson. Med.* 2009; 62(4): 924–934.
279. Zaitsev M, Dold C, Sakas G, Hennig J, Speck O. Magnetic resonance imaging of freely moving objects: prospective real-time motion correction using an external optical motion tracking system. *Neuroimage* 2006; 31(3): 1038–1050.
280. Loktyushin A, Nickisch H, Pohmann R, Scholkopf B. Blind retrospective motion correction of MR images. *Magn. Reson. Med.* 2013; 70(6): 1608–1618.
281. Gallichan D, Marques JP, Gruetter R. Retrospective correction of involuntary microscopic head movement using highly accelerated fat image navigators (3D FatNavs) at 7 T. *Magn. Reson. Med.* 2016; 75(3): 1030–1039.
282. Wen J, Cross AH, Yablonskiy DA. On the role of physiological fluctuations in quantitative gradient echo MRI: implications for GEPC, QSM, and SWI. *Magn. Reson. Med.* 2015; 73(1): 195–203.
283. Versluis MJ, Peeters JM, van Rooden S, van der Grond J, van Buchem MA, Webb AG, van Osch MJ. Origin and reduction of motion and f0 artifacts in high resolution T2*-weighted magnetic resonance imaging: application in Alzheimer's disease patients. *Neuroimage* 2010; 51(3): 1082–1088.
284. Duerst Y, Wilm BJ, Wyss M, Dietrich BE, Gross S, Schmid T, Brunner DO, Pruessmann KP. Utility of real-time field control in T2*-weighted head MRI at 7 T. *Magn. Reson. Med.* 2015 DOI: 10.1002/mrm.25838.
285. Vannesjo SJ, Wilm BJ, Duerst Y, Gross S, Brunner DO, Dietrich BE, Schmid T, Barmet C, Pruessmann KP. Retrospective correction of physiological field fluctuations in high-field brain MRI using concurrent field monitoring. *Magn. Reson. Med.* 2015; 73(5): 1833–1843.
286. Deh K, Nguyen TD, Eskreis-Winkler S, Prince MR, Spincemaille P, Gauthier S, Kovanlikaya I, Zhang Y, Wang Y. Reproducibility of quantitative susceptibility mapping in the brain at two field strengths from two vendors. *J. Magn. Reson. Imaging* 2015; 42(6): 1592–1600.
287. Hinoda T, Fushimi Y, Okada T, Fujimoto K, Liu C, Yamamoto A, Okada T, Kido A, Togashi K. Quantitative susceptibility mapping at 3 T and 1.5 T: evaluation of consistency and reproducibility. *Invest. Radiol.* 2015; 50(8): 522–530.
288. Lin PY, Chao TC, Wu ML. Quantitative susceptibility mapping of human brain at 3 T: a multisite reproducibility study. *Am. J. Neuroradiol.* 2015; 36(3): 467–474.
289. Liu C, Li W. Imaging neural architecture of the brain based on its multipole magnetic response. *Neuroimage* 2013; 67: 193–202.
290. Straub S, Ladd ME, Wetscherek A, Laun FB. On contrast mechanisms in p-space imaging. *Magn. Reson. Med.* 2015; 75(6): 2526–2533.
291. Schweser F, Gomez EDP, Deistung A, Reichenbach JR. What does (multipole) Fourier tensor imaging tell us? – A simulation study. *Proceedings of the 22nd Annual Meeting ISMRM, Milan, Italy, 2014*; 632.
292. Liu C, Li W. STI Suite. Available at: <http://people.duke.edu/~cl160/>; 23 June 2016.
293. Cornell MRI Research Laboratory. Quantitative Susceptibility Mapping Toolbox. Available at: <http://weill.cornell.edu/mri/pages/qsm.html>; 23 June 2016.
294. Sun H. Matlab scripts for QSM. Available at: <https://github.com/sunhongfu/QSM>; 23 June 2016.
295. Bilgic B. Quantitative Susceptibility Mapping Matlab Scripts. Available at: <https://www.martinos.org/~berkin/software.html>; 23 June 2016.